buildings

MDPI

Article

Analysis of Vehicle–Bridge Coupled Vibration and Driving Comfort of a PC Beam–Steel Box Arch Composite System for Autonomous Vehicles

Weiwen Lei [1], Lingbo Wang [1,2,*], Hao Shu [1], Xiaoguang Liu [1,3], Yixiang Liu [1] and Kefan Chen [1]

[1] School of Highway Engineering, Chang'an University, Xi'an 710064, China; 2022221099@chd.edu.cn (W.L.); 2022221081@chd.edu.cn (H.S.); liuxiaoguang@sxjgkg.com (X.L.); 2023121086@chd.edu.cn (Y.L.); chen.kefan@chd.edu.cn (K.C.)
[2] Key Laboratory of Transport Industry of Bridge Detection Reinforcement Technology, Chang'an University, Xi'an 710064, China
[3] SCEGC Mechanized Construction Group Co., Ltd., Xi'an 710032, China
* Correspondence: wanglingbo@chd.edu.cn

Abstract: To investigate the dynamic characteristics of a PC beam–steel box arch composite bridge when the number of loading lanes for autonomous vehicles changes, the vehicle–bridge coupling motion equation was derived and solved iteratively via the Newmark-β method. Joint simulation software based on ANSYS 17.0 and Easy Language was developed to analyze vehicle–bridge coupling and driving comfort. The results showed that the dynamic response is the largest under single-lane conditions, with suspected vehicle–bridge resonance. For multilane conditions, eccentricity is the main factor when the vehicle weight is low, whereas the vehicle weight dominates when it is large. The dynamic response is positively correlated with eccentricity and vehicle weight. With respect to the dynamic amplification factor (DAF), single-lane conditions yield high DAF values for the main beam, main arch, and boom, whereas the main pier has a greater DAF under multilane conditions. Driving comfort is best under single-lane conditions, followed by dual-lane conditions, and worst under three-lane conditions. Speed is the primary influencer of comfort under single-lane conditions, with comfort reduced at higher speeds. Under multilane conditions, both speed and eccentricity affect comfort, with speed being the dominant factor. The calculated impact coefficient significantly exceeds the standard values, suggesting that separate impact coefficients should be set for each load-bearing component. These findings, combined with driving comfort analysis, provide valuable references for the setting of speed limits and the design and maintenance of such bridges under autonomous vehicle loads.

Keywords: bridge engineering; beam–arch composite bridge; steel–concrete composite system; vehicle–bridge coupling; driving comfort; autonomous vehicles

Academic Editor: Fabrizio Gara

Received: 13 February 2025
Revised: 10 April 2025
Accepted: 14 April 2025
Published: 21 April 2025

Citation: Lei, W.; Wang, L.; Shu, H.; Liu, X.; Liu, Y.; Chen, K. Analysis of Vehicle–Bridge Coupled Vibration and Driving Comfort of a PC Beam–Steel Box Arch Composite System for Autonomous Vehicles. *Buildings* **2025**, *15*, 1385. https://doi.org/10.3390/buildings15081385

1. Introduction

With the rapid development of highway construction, composite system bridges are widely used in construction, renovation, and reinforcement. The advantages of these materials are that they have a high bearing capacity, have a large span, and are economical. The most common composite system bridge types are beam–arch composite systems and steel–concrete composite systems. However, owing to the complexity of the structural system and materials, the vehicle–bridge coupled dynamic response under dynamic loads is still unclear. In studies of vehicle–bridge coupled vibration, the impact coefficient is the main evaluation index and design index used to evaluate dynamic loads. Many scholars

have reported that there is no uniform approach for calculating the impact coefficient, and the standards of various countries underestimate the impact coefficient in cases with bridge vibration [1,2].

In recent years, scholars have gradually shifted their research on vehicle–bridge coupling to complex bridge types, such as combined-system beam bridges [3], cable structures, and special bridge types, and have established various complex simulation methods to study dynamic responses. Gao et al. [4] established a steel–concrete composite beam bridge model and studied the influence of different factors on the dynamic response of the bridge. Zhang et al. [5] studied the effect of the ARID system on the stability of arch rib structures. Yang et al. [6] established random traffic flow and convoy models to analyze the effects of different parameters on the vehicle–bridge coupled vibration of cable-stayed bridges. Guo et al. [7] established a vehicle–bridge coupled model for predicting the dynamic response and impact coefficient of long-span curved beam bridges. Xie et al. [8] proposed a finite element method based on vehicle–bridge coupling vibration theory to evaluate concrete truss arch bridges. Li Ximei et al. [9] analyzed the vertical vibration of a double I-beam–concrete composite beam bridge with vehicle–bridge coupling. The above studies focused on the dynamic responses of complex bridge structures and ignored vehicle comfort. Wang et al. [10] proposed a method to identify structural vibration displacement using lightweight convolutional neural networks, and selected a cable-stayed bridge model for experiments to verify the accuracy of the algorithm. Zhou et al. [11] proposed a hybrid deep learning model architecture that combines physical information and data-driven approaches to identify vehicle time-varying parameters and describe vehicle lateral dynamics. Similarly, Chen et al. [12] proposed a neural network model that combines physical and attentional mechanisms to simulate the lateral dynamics of vehicles. Liang et al. [13] proposed a bootstrapped deep Q-Network to achieve adaptive decision-making of autonomous vehicles (AVs). Their simulations demonstrate that the proposed integrated framework can guide AVs to take safe actions while guaranteeing high-speed cruising performance.

Driving comfort refers to the degree of discomfort experienced by the occupants of a vehicle while driving. Vehicle–bridge coupled vibration may aggravate the vibration of the vehicle and even cause the vehicle to jump and move significantly. The driving comfort of passengers in vehicles moving at high speeds on large-span bridges has become increasingly studied.

In current research, considering that the impact of vehicle–bridge coupled vibration on driving comfort has become important in bridge design [14], researchers usually use numerical methods to calculate the dynamic responses of vehicles and bridges. They then calculate the parameter values with reference to relevant standards for driving comfort and finally evaluate driving comfort. Gao et al. [15] proposed a frequency-domain-based dynamic analysis method to assess the interaction between trains and beams and evaluated train vibrations by using a ride comfort index based on weighted triple-band acceleration. Kırbaş Ufuk [16] obtained vibration measurements according to the ISO2631 standard and mathematically modeled the relationships among the whole-body vibration exposure of a certain vehicle model, the driving speed, and the international roughness index (IRI). Li et al. [17] used the maximum vibration acceleration limit and the Sperling index to evaluate the riding comfort and safety of a high-temperature superconducting (HTS) maglev train under the influence of an open-air crosswind. Zhang et al. [18,19] developed a vortex–vehicle–bridge coupled system in the multimode locking area of a double-box deck and used the overall vibration total value (OVTV) in the ISO2631-1 standard to study the effects of vortex-induced vibration and turbulence on riding comfort. Liu et al. [20] studied the influence of the multiaxial fatigue load spectrum of automobile parts on driving

comfort. Wu et al. [21] established a dynamic analysis framework for a vehicle–bridge coupled system under ice-induced vibration conditions and used ISO2631-1 (1997) [22] and ISO2631-1 (1985) [23] to evaluate driving comfort.

The abovementioned studies focused on the driving comfort of traditional vehicles. However, with the development of the automotive industry, autonomous vehicles, which are equipped with many high-precision sensors, cameras and other electronic devices, can quickly, accurately, and comprehensively integrate information about the surrounding driving environment. This information is then used for system analysis to make decisions that yield the highest benefits. In this way, autonomous vehicles can effectively address issues such as long reaction times, limited field of vision, and fatigue during long-distance driving, which are associated with the limited driving capabilities of humans. The Ministry of Transport issued the Guidelines for Highway Engineering Facilities to Support Automated Driving Technology in 2023 as a recommended industry standard for highway engineering, revealing the future development trends of automated vehicles (AVs) and connected vehicles (CVs). With the continuous development and improvement of autonomous driving technology, the future transportation environment will be a fully autonomous driving environment [24]. Ling et al. [25] studied the dynamic response of an automated truck platoon (ATP) on high-speed bridges. The results showed that, owing to the superposition effect, the dynamic impact of the ATP on the bridge was significantly greater than that of a single truck. However, none of these studies explored the driving comfort of autonomous vehicles.

In summary, the dynamic analysis of vehicle–bridge coupling for complex bridge types and the evaluation of driving comfort for autonomous vehicles are still in the exploratory stage, especially for beam–arch composite bridges and steel–concrete composite structures. The beam–arch composite bridge combines the advantages of beams and arches, effectively distributing loads and adapting to complex terrains and traffic demands. In recent years, it has been widely used for long-span bridges and in the reinforcement and renovation of old bridges. Owing to the main load-bearing components, including the main beam and main arch, the dynamic behavior of beam–arch composite bridges is relatively complex. The interaction between the main beam and arch ribs leads to unique vibration characteristics [26]. Studying the dynamic response of this type of bridge is highly important for optimizing structural design and improving safety and comfort. With the rapid development of autonomous driving technology, fully autonomous environments have become a trend in transportation development. Therefore, research on the dynamic performance of bridge structures and driving comfort under autonomous vehicle loads is particularly important.

The innovation of this study lies in addressing the limitations of current research in vehicle–bridge coupled dynamic response analysis, particularly the lack of comprehensive consideration of the combined effects of multiple factors. A new analytical framework is proposed, which not only considers the individual effects of factors such as vehicle number, speed, driving position, and lane count but also systematically links their combined effects for analysis. This fills a gap in existing research and provides a comprehensive analytical perspective. Specifically, this study focuses on a long-span PC beam–steel box arch composite bridge, and the dynamic response of the bridge structure under the combined effects of multiple factors is assessed on the basis of changes in the number of loading lanes for autonomous vehicles. The driving comfort of passengers in autonomous vehicles is also evaluated. Through this research, we aim to provide practical reference recommendations for determining impact coefficients and evaluating driving comfort under complex driving conditions for beam–arch composite bridges and steel–concrete composite structures, thereby promoting further research in this field.

2. Basic Theory

2.1. Theory of Vehicle–Bridge Coupled Vibration Analysis

Vehicles traveling on highway bridges will cause bridge vibration, which in turn affects vehicle vibration. The vehicle and bridge are regarded as two subsystems, and a multi degree-of-freedom vehicle–bridge coupled vibration system is formed through displacement coordination and force balance constraints for analysis.

First, according to finite element theory, the bridge vibration equation is established as follows:

$$[\boldsymbol{M_b}]\left\{\ddot{\boldsymbol{Z}}_b\right\} + [\boldsymbol{C_b}]\left\{\dot{\boldsymbol{Z}}_b\right\} + [\boldsymbol{K_b}]\{\boldsymbol{Z_b}\} = \{\boldsymbol{F_b}\} \tag{1}$$

Second, the vehicle vibration equation is established according to the D'Alembert principle and finite element theory as follows:

$$[\boldsymbol{M_v}]\left\{\ddot{\boldsymbol{Z}}_v\right\} + [\boldsymbol{C_v}]\left\{\dot{\boldsymbol{Z}}_v\right\} + [\boldsymbol{K_v}]\{\boldsymbol{Z_v}\} = \{\boldsymbol{F_v}\} \tag{2}$$

where $[\boldsymbol{M_b}]$, $[\boldsymbol{C_b}]$, and $[\boldsymbol{K_b}]$ are the mass, damping, and stiffness matrices of the bridge model, respectively; $\{\boldsymbol{Z_b}\}$, $\left\{\dot{\boldsymbol{Z}}_b\right\}$, and $\left\{\ddot{\boldsymbol{Z}}_b\right\}$ are the displacement, velocity, and accelerator vector matrices of the bridge model, respectively; $\{\boldsymbol{F_b}\}$ is the external force vector matrix of the bridge; $[\boldsymbol{M_v}]$, $[\boldsymbol{C_v}]$, and $[\boldsymbol{K_v}]$ are the mass, $\{\boldsymbol{F_v}\}$ damping, and stiffness matrices of the vehicle space model, respectively; and $\{\boldsymbol{Z_v}\}$, $\left\{\dot{\boldsymbol{Z}}_v\right\}$, and $\left\{\ddot{\boldsymbol{Z}}_v\right\}$ are the displacement, velocity, and accelerator vector matrices of the bridge model, respectively.

For the vehicle system, considering eccentric effects and torque in the vehicle subsystem equation of motion $[\boldsymbol{M_v}]\left\{\ddot{\boldsymbol{Z}}_v\right\} + [\boldsymbol{C_v}]\left\{\dot{\boldsymbol{Z}}_v\right\} + [\boldsymbol{K_v}]\{\boldsymbol{Z_v}\} = \{\boldsymbol{F_v}\}$, according to existing research [27,28], the key to vehicle–bridge coupling is establishing the contact relationship between the wheels and bridge deck. When a vehicle travels eccentrically, the vehicle load not only causes bending effects on the bridge but also induces torsional effects. The contact force between the wheel and bridge deck can be expressed as

$$\{\boldsymbol{F_a}\} = -\{\boldsymbol{F_v}\} = \{\boldsymbol{R}\}\cdot\{\boldsymbol{F_c}\}$$

$$\{\boldsymbol{F_a}\} = \left\{\boldsymbol{T_a^{torsional}}\right\} + \left\{\boldsymbol{F_a^{vertical}}\right\}$$

where $\{\boldsymbol{F_a}\}$ represents the contact force between wheel and bridge deck, $\{\boldsymbol{F_c}\}$ is the wheel–bridge contact force vector, $\{\boldsymbol{R}\}$ is the mapping matrix that transfers contact forces from contact points to bridge nodes, $\left\{\boldsymbol{T_a^{torsional}}\right\}$ is the torsional force moment matrix caused by eccentricity, and $\left\{\boldsymbol{F_a^{vertical}}\right\}$ is the vertical force moment matrix.

$$F_a^{vertical}(x,t) = \sum_{i=1}^{n} F_i(t)\cdot\delta[x - x_i(t)]$$

$$T_a^{torsional}(x,t) = \sum_{i=1}^{n} e_i\cdot F_i(t)\cdot\delta[x - x_i(t)]$$

where n is the number of wheels on the vehicle; $F_i(t)$ is the dynamic contact force of the i-th wheel at a given time; δ is the Dirac function, indicating the position where the force acts; $x_i(t)$ is the position of the i-th wheel at a given time; e_i is the lateral eccentric distance from the th wheel to the bridge centerline.

In the beam–arch composite bridge, the beam and arch are the main load-bearing components, and the displacement function vectors $\{\boldsymbol{Z_{b1}}\}$ and $\{\boldsymbol{Z_{b2}}\}$ of the beam and arch need to be calculated. The solution process is divided into the following four steps.

First, the global dynamic model of the beam–arch composite bridge is established, as shown in Figure 1.

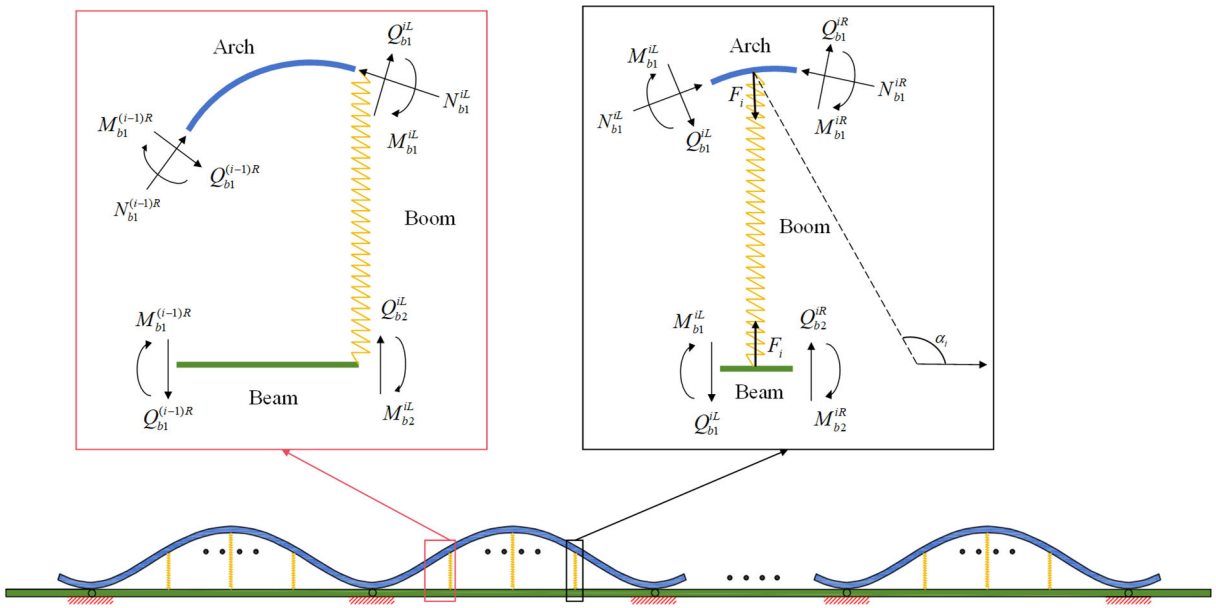

Figure 1. Mechanical model of the beam–arch composite bridge.

Using the separation of variables method and force balance conditions, the expressions of the arch radial displacement function $\boldsymbol{Z}_{b1}$ and the beam vertical displacement function $\boldsymbol{Z}_{b2}$ are obtained:

$$\boldsymbol{Z}_{b1} = \begin{bmatrix} \boldsymbol{U}_{b1} \\ \boldsymbol{V}_{b1} \\ \boldsymbol{\theta}_{b1} \\ \boldsymbol{M}_{b1} \\ \boldsymbol{Q}_{b1} \\ \boldsymbol{N}_{b1} \end{bmatrix} = \begin{bmatrix} \boldsymbol{T}_{1,1} & \boldsymbol{T}_{1,2} & \boldsymbol{T}_{1,3} & \boldsymbol{T}_{1,4} & \boldsymbol{T}_{1,5} & \boldsymbol{T}_{1,6} \\ \boldsymbol{T}_{2,1} & \boldsymbol{T}_{2,2} & \boldsymbol{T}_{2,3} & \boldsymbol{T}_{2,4} & \boldsymbol{T}_{2,5} & \boldsymbol{T}_{2,6} \\ \boldsymbol{T}_{3,1} & \boldsymbol{T}_{3,2} & \boldsymbol{T}_{3,3} & \boldsymbol{T}_{3,4} & \boldsymbol{T}_{3,5} & \boldsymbol{T}_{3,6} \\ \boldsymbol{T}_{4,1} & \boldsymbol{T}_{4,2} & \boldsymbol{T}_{4,3} & \boldsymbol{T}_{4,4} & \boldsymbol{T}_{4,5} & \boldsymbol{T}_{4,6} \\ \boldsymbol{T}_{5,1} & \boldsymbol{T}_{5,2} & \boldsymbol{T}_{5,3} & \boldsymbol{T}_{5,4} & \boldsymbol{T}_{5,5} & \boldsymbol{T}_{5,6} \\ \boldsymbol{T}_{6,1} & \boldsymbol{T}_{6,2} & \boldsymbol{T}_{6,3} & \boldsymbol{T}_{6,4} & \boldsymbol{T}_{6,5} & \boldsymbol{T}_{6,6} \end{bmatrix} \begin{bmatrix} \boldsymbol{C}_1 \\ \boldsymbol{C}_2 \\ \boldsymbol{C}_3 \\ \boldsymbol{C}_4 \\ \boldsymbol{C}_5 \\ \boldsymbol{C}_6 \end{bmatrix} \tag{3}$$

$$\boldsymbol{Z}_{b2} = \begin{bmatrix} \boldsymbol{V}_{b2} \\ \boldsymbol{\theta}_{b2} \\ \boldsymbol{M}_{b2} \\ \boldsymbol{Q}_{b2} \end{bmatrix} = \begin{bmatrix} \boldsymbol{T}_{7,7} & \boldsymbol{T}_{7,8} & \boldsymbol{T}_{7,9} & \boldsymbol{T}_{7,10} \\ \boldsymbol{T}_{8,7} & \boldsymbol{T}_{8,8} & \boldsymbol{T}_{8,9} & \boldsymbol{T}_{8,10} \\ \boldsymbol{T}_{9,7} & \boldsymbol{T}_{9,8} & \boldsymbol{T}_{9,9} & \boldsymbol{T}_{9,10} \\ \boldsymbol{T}_{10,7} & \boldsymbol{T}_{10,8} & \boldsymbol{T}_{10,9} & \boldsymbol{T}_{10,10} \end{bmatrix} \begin{bmatrix} \boldsymbol{C}_7 \\ \boldsymbol{C}_8 \\ \boldsymbol{C}_9 \\ \boldsymbol{C}_{10} \end{bmatrix} \tag{4}$$

Since the beam–arch is coupled via the boom connection, the overall matrix equation is obtained by combining Equations (3) and (4):

$$\boldsymbol{Z}_{\boldsymbol{b}} = \boldsymbol{TC} \tag{5}$$

where U_{b1} represents the tangential displacement of the arch, V_{b1} represents the radial displacement of the arch, θ_{b1} represents the rotation angle of the arch, M_{b1} represents the bending moment of the arch, N_{b1} represents the axial force of the arch, V_{b2} represents the vertical displacement of the beam, θ_{b2} represents the rotation angle of the beam, M_{b2} represents the bending moment of the beam, Q_{b2} represents the shear force of the beam, $T_{1,1\sim6,6}$ and $T_{7,7\sim10,10}$ represent the displacement functions of the arch and beam, respectively, and the internal force function corresponding coefficient is $C_1 \sim C_{10}$. The position front parameter Z_b is the position state vector of any section of the beam–arch segment, C is the integral vector constant, and T is the overall coefficient matrix of the beam–arch segment.

Second, based on the analysis of a single beam–arch section of any span structure in a bean–arch composite bridge, for the leftmost cross-sectional position of any beam–arch section, the central angle $\varphi = 0$ corresponding to the arch section and the length $x = 0$ corresponding to the beam section are used, and the central angle $\varphi = 0$ and length $x = 0$ in T are as follows:

$$\boldsymbol{Z_b^{(i-1)R} = T^0 C} \tag{6}$$

$$\boldsymbol{Z_b^{iL} = U^i Z_b^{(i-1)R}} \tag{7}$$

where $(T^0)^{-1}$ is the inverse of the coefficient matrix when the central angle of the arch segment is 0 and the length of the beam segment is 0. U^i represents the transfer matrix for the i-th beam–arch segment. $Z_b^{(i-1)R}$ is the initial position of the i-th beam–arch segment, and Z_b^{iL} is the end position of the i-th beam–arch segment.

Then, the local position node of the i-th boom is selected for force analysis, and the equilibrium equation of the local position node of the i-th hanger is as follows:

$$\boldsymbol{Z_b^{iR} = K^i Z_b^{iL}} \tag{8}$$

where K^i is the point transfer matrix at the local position of the i-th boom and Z_b^{iR} is the beam–arch end state vector at the rightmost position of the i-th boom.

On the basis of the derivation of the field matrix and the point matrix, Equations (7) and (8) are combined to yield the following expression:

$$\boldsymbol{Z_b^{iR} = TZ_b^{(i-1)R}} \tag{9}$$

where $\boldsymbol{T^i = K^i U^i}$ represents the unit transfer matrix of the i-th beam–arch segment corresponding to the transformation from the rightmost cross-sectional position of the i-th boom to the rightmost cross-sectional position of the i-th boom.

On the basis of the transfer matrix principle, the two spans are connected by rigid coupling, and the multi-span beam–arch composite bridge is split into multiple single-span beam–arch composite bridges. The overall transfer matrices are calculated and merged, and then the overall eigenvalue equation is derived through the natural boundary conditions and coupled boundary conditions at both ends of the system. By multiplying the unit matrices for the beam–arch transfer sections connected end to end, the overall transfer matrix of the single-span arch bridge can be obtained:

$$\boldsymbol{T = \prod_{i=1} T^i} \tag{10}$$

Finally, with the displacement coordination and the contact force being opposite in direction and equal in magnitude as the joint conditions, the Newmark-β method is used to iteratively solve the coupled equations, and the displacement in the calculation process is controlled to achieve convergence. In vehicle–bridge coupled solutions, the Newmark-β method is often combined with the separation iteration method, performing time integration and coupled processing at each time step to ensure the stability of the computational results. Compared with other integration methods, the Newmark-β method can guarantee unconditional stability by adjusting parameters, ensuring computational accuracy. It is suitable for nonlinear problems, and its algorithm is simple and easy to implement. It can be combined with the finite element method for bridge modeling, making it flexible and efficient in engineering applications.

The convergence conditions are as follows:

$$\frac{|\boldsymbol{Z}_{t+\Delta t} - \boldsymbol{Z}_t|}{|\boldsymbol{Z}_t|} \leqslant \xi \tag{11}$$

where $\boldsymbol{Z}_{t+\Delta t}$ and Z_t are the displacement values of the contact point between the bridge and the vehicle at time t and time $t + \Delta t$, respectively, and ξ is the convergence control index, which is set to 0.01.

In the coupled vibration analysis of highway bridges and vehicle bridges, the dynamic amplification factor (DAF) is typically used to evaluate the dynamic response amplification level of the bridge under the action of vehicle loads, which is calculated according to Equation (12):

$$DAF = \frac{Y_{d\max}}{Y_{j\max}} \tag{12}$$

where Y_{dmax} is the extreme value of the dynamic response and Y_{jmax} is the extreme value of the static response.

2.2. Theory of Driving Comfort Analysis and Evaluation

Autonomous vehicles rely on sensors to perceive the environment, enabling highly automated driving. This reduces human error and enhances driving safety as well as the comfort experience of passengers. The speed range of autonomous vehicles is determined by algorithms, ensuring precise control within the safe driving speed limit of the road. Moreover, they maintain a stable state during cases with vehicle condition warnings and long-distance driving.

Lprecipe et al. [29] reported that the ISO2631 method is suitable for evaluating driving comfort at low speeds. The speed range studied in this paper is 60–100 km/h, which is relatively low, so the ISO2631 method is used to evaluate driving comfort. In the ISO2631-1-1997 method, the human sitting posture under vibration conditions is used as the basis of the analysis model (Figure 2). The analysis focuses on the vertical vibration, lateral vibration, and pitch vibration of the vehicle body, considering 12 degrees of freedom.

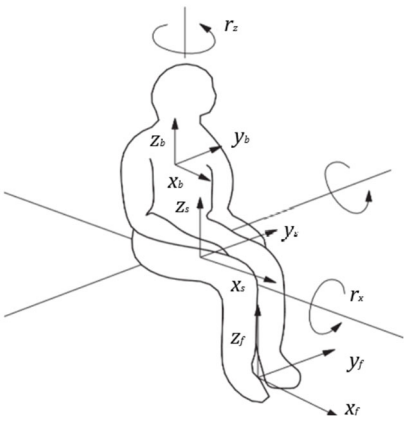

Figure 2. Coordinate system of the human body while sitting.

The total weighted root mean square (RMS) of acceleration is used as the evaluation index of driving comfort. In data processing, weighting filters are applied to emphasize the 4–8 Hz frequency range, to which humans are most sensitive to vibrations. A high RMS value indicates pronounced vibrations perceived by the human body, leading to low comfort.

The RMS is calculated via the following formula:

$$a_v = \left[\sum_{i=1}^{N} (k_i a_{\omega i})^2\right]^{1/2} \tag{13}$$

Vehicle vibration mainly consists of vertical vibration, lateral vibration, and pitch vibration of the vehicle body, so Equation (12) can be simplified as follows:

$$a_v = \left[(k_1 a_{\omega 1})^2 + (k_2 a_{\omega 2})^2 + (k_3 a_{\omega 3})^2\right]^{1/2} \tag{14}$$

where N is the number of degrees of freedom; k_i is the weighting coefficient of the RMS (k_1, k_2, and k_3 are the weighting coefficients of the vertical, pitch, and lateral RMSs, respectively); and $a_{\omega i}$ is the acceleration of the i-th degree of freedom.

The relationships between the RMS and the driving comfort level are shown in Table 1.

Table 1. Relationships between the driving comfort level and the RMS.

RMS (m/s^2)	Driving Comfort Rating
<0.315	Not uncomfortable
0.315~0.63	A bit uncomfortable
0.5~1	Somewhat uncomfortable
0.8~1.6	Uncomfortable
1.25~2.5	Very uncomfortable
>2.0	Extremely uncomfortable

3. Vehicle–Bridge Coupled Analysis Model

3.1. Subsection

This paper describes a two-way, six-lane continuous beam-arch composite bridge located in Shaanxi Province. The bridge spans 90 m + 170 m × 4 + 90 m. The main beam consists of a prestressed concrete single-box, single-chamber design with a width of 41.6 m, and a cross-section of the main beam is illustrated in Figure 3. The stiffened steel box arch is constructed from Q345qD steel, featuring a rise of 27 m and a rise-to-span ratio of approximately 1:6.296. Additionally, there are 11 pairs of hangers for each single main span. A section of the steel box arch is depicted in Figure 4.

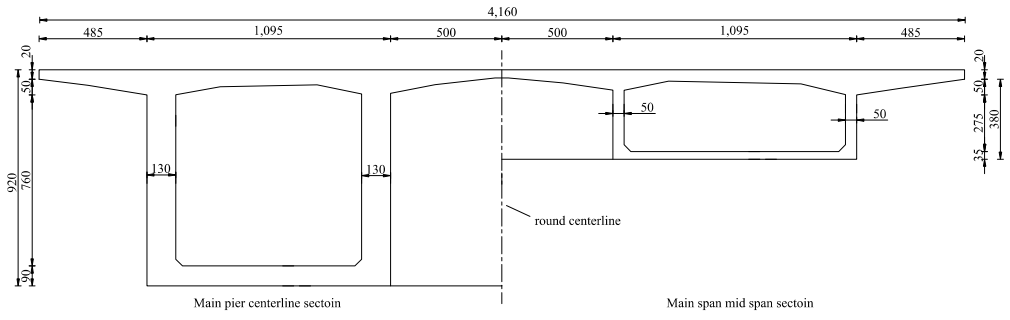

Figure 3. Main beam section (unit: cm).

In this study, the bridge calculation model was established via the general finite element software ANSYS, as shown in Figure 5. In the ANSYS model of the bridge, the main girder and main piers were modeled via BEAM188 elements, the hangers were modeled via LINK10 elements, and the arch ribs were modeled via BEAM44 elements. The secondary dead load was modeled via MASS21 elements. The sectyp, secdata, secwrite, and secoffset commands were used to define two adjacent sections numbered i and i + 1,

respectively, and a *loop* command was used to generate continuously varying cross-sections in batches. A rigid connection was applied between the main girder and the main piers. The connections among the hangers, the main girder, and the main arch were coupled via the CP command stream.

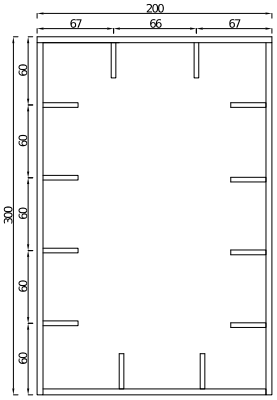

Figure 4. Steel box arch section (unit: cm).

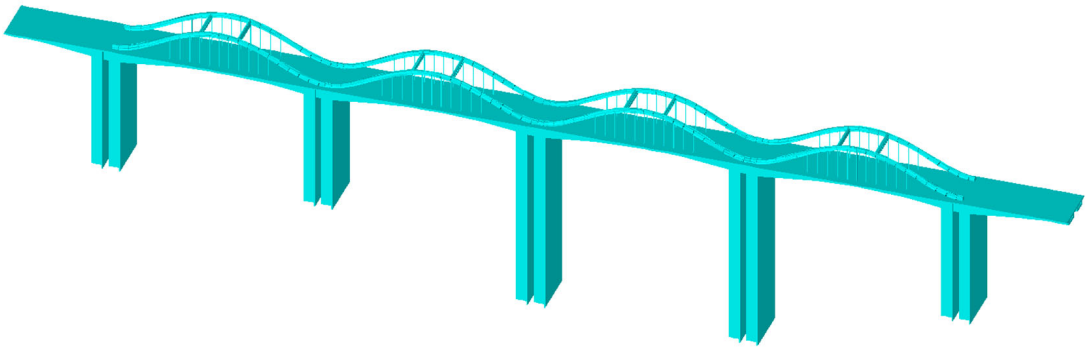

Figure 5. ANSYS finite element model of the bridge.

In establishing the bridge model, the left end of the main beam constrains the z, y direction displacement degrees of freedom and rotation around the x-axis, while the right end constrains the z, y direction displacement degrees of freedom and rotation around the x and y axes. In the model, the left end of the bridge only constrains Uz, Uy, and $ROTx$, allowing longitudinal displacement (Ux), simulating a unidirectional movable support, while the right end additionally constrains $ROTy$, limiting rotation around the numerical axis and increasing overall stability. The impact of this modeling approach on the impact factor is as follows: The left support allows longitudinal displacement, reducing the overall stiffness of the structure. Different constraints at the left and right ends lead to asymmetric vibration modes, causing significant differences in impact factors at different positions. When vehicles enter from the lower stiffness (left end) direction, they cause larger impact factors. Our modeling considered the actual conditions of the supporting project, combined with influencing factors of the impact factor, setting vehicles to enter from the left end.

To ensure the accuracy of the ANSYS bridge model and its consistency with design results, we compared the model calculation data with the design drawing results. We extracted the bending moments of the main load-bearing components, specifically the main girders and main arches, under dead load conditions and plotted comparative diagrams of bending moments for different components, as shown in Figures 6 and 7.

The results demonstrate that the deviations between our bridge model calculations and the theoretical design values are all within the engineering allowable range of 5%, verifying the computational accuracy of the established ANSYS model. This validation

ensures a reliable foundation for subsequent dynamic response analysis and provides solid verification evidence for the numerical method proposed in this study.

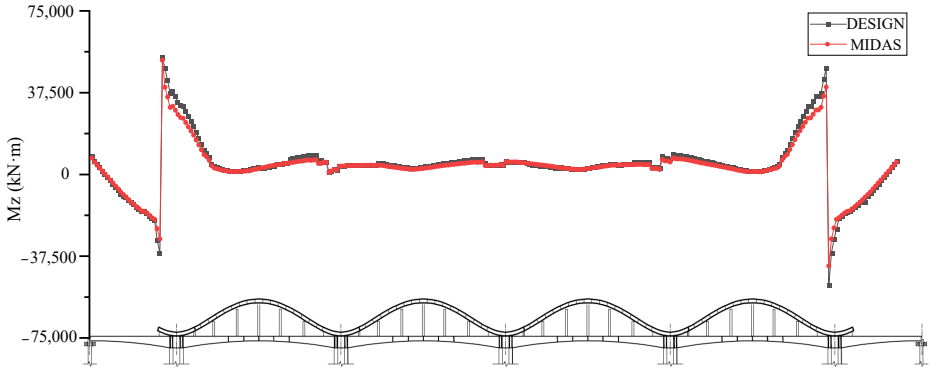

Figure 6. Comparison of main girder bending moments.

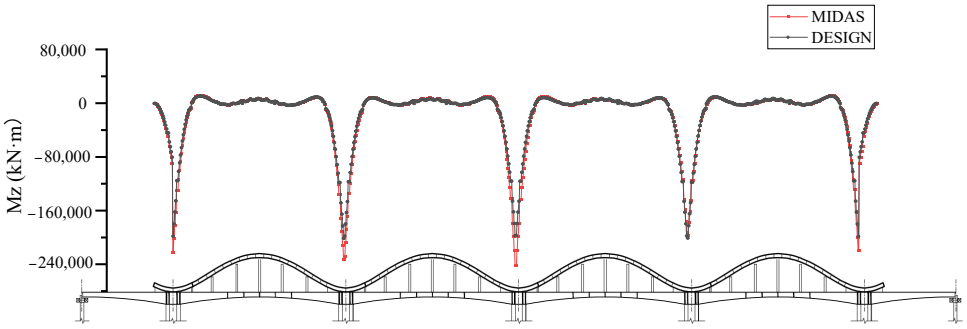

Figure 7. Comparison of main arch bending moments.

Before initiating the model computation, computational options must be configured. In this case study on vehicle–bridge coupled vibration, which investigates the dynamic response of the vehicle and bridge structure under time-varying loads, the core characteristic lies in the rapid temporal evolution of the system's state (e.g., displacements, stresses). This necessitates analyzing the time-history response of the structure. Consequently, the ANSYS analysis type is set to Transient Analysis. Additionally, large deformation effects are enabled to account for geometric nonlinearities caused by structural configuration changes. Finally, the Newmark-β method is employed to discretize the dynamic equations, while the Newton–Raphson method is configured to handle nonlinearities during contact iterations. After the calculation, the model converged, and the total displacement cloud diagram obtained is shown in Figure 8. To further verify the reliability of the model, the simulation results of this study were compared with the measurements in a published journal paper [30]. The simulation results are in good agreement with the measured data.

According to the General Specification for Highway Bridge and Culvert Design (JTG D60-2015 [31]), the impact factor is related to the natural frequency of the bridge, as shown in Equation (15). Table 2 shows the first 10 natural frequencies and corresponding modes of the supporting project.

$$\begin{cases} \mu = 0.05 & f \le 1.5\ \text{Hz} \\ \mu = 0.1767 \ln f - 0.0157 & 1.5\ \text{Hz} \le f \le 14\ \text{Hz} \\ \mu = 0.45 & f \ge 14\ \text{Hz} \end{cases} \tag{15}$$

Table 2 shows that the first 10 natural frequencies of the bridge are f_i < 1.5 Hz $(i = 1, 2 \ldots, 10)$, so the recommended value of the impact coefficient of the bridge is determined to be 0.05.

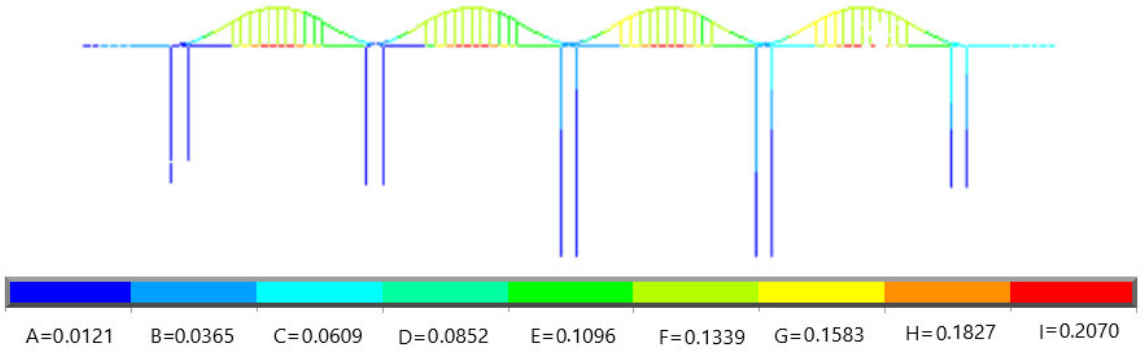

Figure 8. Total displacement cloud diagram.

Table 2. The first 10 natural frequencies and corresponding vibration modes.

Mode Number	Frequency	Modal Description
1	0.23786	System vertical drift
2	0.30936	Horizontal drift in the plane of the main beam
3	0.41370	#2, #4 span antisymmetric transverse bending
4	0.43907	#1, #4 symmetrical horizontal bending
5	0.44674	Antisymmetric transverse bending of the main beam
6	0.46699	Horizontal drift in the plane of the main beam
7	0.49639	#2, #4 span antisymmetric transverse bending
8	0.61501	Main beam bending
9	0.64493	Main beam bending
10	0.77034	#3 vertical bending

3.2. Vehicle Model and Parameters

With the development of the electric vehicle and intelligent driving industries, the distributed-wheel motor drive architecture has been widely applied because of its advantages, such as a simple transmission chain, low power loss, short response time, precise real-time control effect, and diverse and easy-to-develop control algorithms [32]. Most of the existing power models of in-wheel-motor-driven vehicles are 1/4 vehicle models or half-vehicle models. To comprehensively analyze the vertical, pitching, and rolling vibrations of this vehicle type, as well as the relationships between the vehicle body and wheels, a spatial multi degree-of-freedom full-vehicle model is established.

Notably, a seven-degree-of-freedom two-axis spatial vehicle model and a nine-degree-of-freedom three-axis spatial vehicle model are used to simulate two-axle cars and two-axle trucks and three-axle trucks, respectively. The nine-degree-of-freedom three-axis spatial vehicle model is shown in Figure 9.

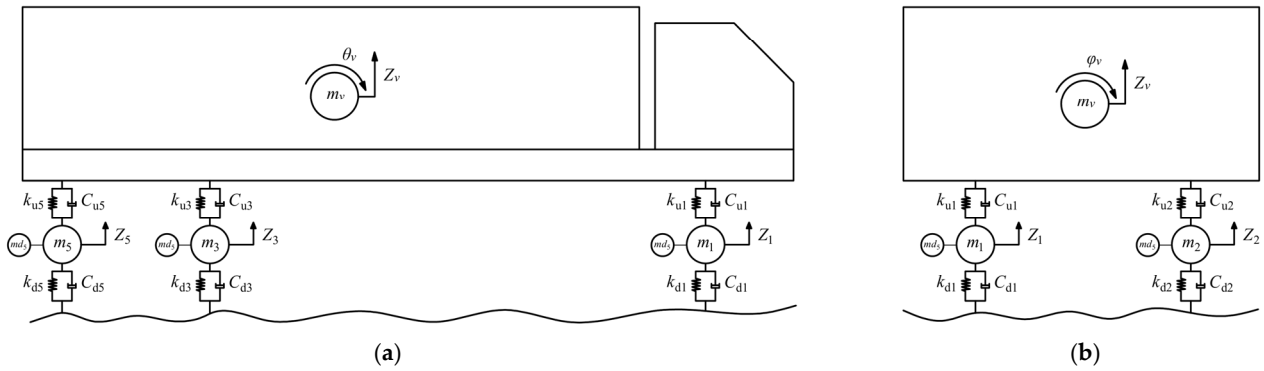

(**a**) (**b**)

Figure 9. Nine-degree-of-freedom three-axis spatial vehicle model: (**a**) left side view, and (**b**) front view.

The meanings and specific values of the parameters in the figure are shown in Table 3.

Table 3. Vehicle model parameters.

	Two-Axle Cars	Two-Axle Trucks	Three-Axle Trucks
Front axle wheelset mass $m_1(m_2)$	150 kg	725.4 kg	297 kg
Center axle wheelset quality $m_3(m_4)$	/	/	466 kg
Rear axle wheelset mass $m_5(m_6)$	200 kg	725.4 kg	466 kg
Body mass m_c	1535 kg	24,808 kg	30,542 kg
Longitudinal moment of inertia of the vehicle body I_{c1}	25,000 kg·m^2	172,160 kg·m^2	55,259 kg·m^2
Lateral moment of inertia of the vehicle body I_{c2}	1731 kg·m^2	31,496 kg·m^2	6893 kg·m^2
Spring rate of front axle $K_{u1}(K_{u2})$	100,000 N/m	727,812 N/m	630,000 N/m
Spring rate of middle axle $K_{u3}(K_{u4})$			790,000 N/m
Spring rate of rear axle $K_{u5}(K_{u6})$	300,000 N/m	1,969,034 N/m	790,000 N/m
Front axle lower spring rate limit $K_{d1}(K_{d2})$	100,000 N/m	1,972,900 N/m	2,800,000 N/m
Middle axle lower spring rate limit $K_{d3}(K_{d4})$	/	/	2,800,000 N/m
Rear axle lower spring rate limit $K_{d5}(K_{d6})$	302,000 N/m	4,735,000 N/m	2,800,000 N/m

3.3. Autonomous Vehicle Model

According to the working principle of the hub motor, there are four main types of motor structures: permanent magnet synchronous motors, DC motors, asynchronous motors, and switched reluctance motors [33]. Switched reluctance motors are characterized by high efficiency, high power density, and a wide speed range and are currently widely used in hub-driven electric vehicles. Therefore, for the vehicle model in this paper, a switched reluctance motor is selected for power analysis. The four-phase 8/6-pole switched reluctance motor and its switching circuit are shown in Figure 10.

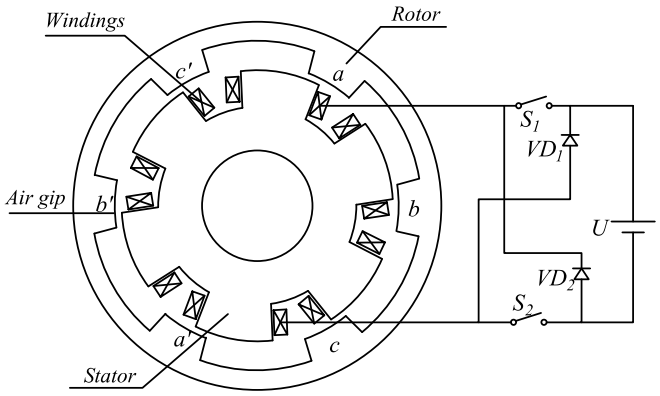

Figure 10. Structure of the four-phase 8/6-pole switched reluctance motor.

Under certain assumptions, the vertical force of the one-way rotor at a certain moment is as follows [34]:

$$F_{vj}(t) = \begin{cases} A\sin\theta + B\cos\theta & nT_R < t < nT_R + T_1 \\ 0 & nT_R + T < t < (n+1)T_R \end{cases} \quad (16)$$

$$A = \frac{i^2}{2}\frac{L_{min} + K\omega(t - nT_R)}{\sqrt{b^2 + (r\omega)^2[T_1 - (t - nT_R)]^2}},\ B = \frac{Ki^2}{2R} \quad (17)$$

$$\theta = \theta_{int} + \omega t + \phi, b = (R - r) - e\cos\phi \quad (18)$$

where i is the motor current; L_{min} is the minimum inductance; b is the motor air gap; e is the eccentricity of the stator and the rotor; K is the rising slope of the inductance; R is the inner radius of the rotor; r is the outer radius of the stator; TR is the rotation period of the single-phase rotor; ω is the angular speed of motor rotation; θ_{int} is the initial position of each phase rotor; and ϕ is the phase angle of each stator winding.

The overall vertical excitation of the motor is the sum of the single-phase rotor vertical forces, that is,

$$F_{\mathrm{vd}} = F_{va} + F_{\mathrm{v}b} + F_{\mathrm{v}c} + F_{\mathrm{v}a'} + F_{\mathrm{v}b'} + F_{\mathrm{v}c'} \tag{19}$$

where $F_{\mathrm{v}a}$, $F_{\mathrm{v}b}$, $F_{\mathrm{v}c}$, $F_{\mathrm{v}a'}$, $F_{\mathrm{v}b'}$, and $F_{\mathrm{v}c'}$ are the vertical forces of the single-phase rotor, and a, a', b, b', c, and c' are the corresponding rotors in the hub motor.

3.4. Bridge Deck Roughness Simulation

MATLAB R2022B was used to simulate the roughness of the bridge surface via Fourier inverse transform:

$$|X_i| = \sqrt{\frac{N}{2\Delta l} G_x(n_i)} \quad (i = 0, 1, 2, \cdots, \frac{N}{2}) \tag{20}$$

where $|X_k|$ is the signal modulus. $\Delta n = \frac{1}{L}$, where L is the bridge deck length. $n_i = i\Delta n$, where Δn is the spatial frequency resolution. $G_x(n_i)$ is the power spectral density function in discrete form, $G_x(n_i)\ \Delta l$ is the sampling interval, and N is the number of sampling frequency bands.

The project studied in this paper is based on a highway. According to China's "Highway Maintenance Quality Standards" (Table 4), to ensure the maintenance quality of highways, the maintenance quality index (MQI) should be consistently maintained above 80. On the basis of this standard, this study adheres to the principle of the "most unfavorable" condition and selects the B grade for the bridge deck roughness level. High roughness grades do not accurately reflect the most unfavorable conditions for vehicle–bridge interactions, whereas low grades do not meet highway maintenance standards and are inconsistent with actual conditions. Additionally, the selection of B-grade roughness conforms to the classification of road surface evenness from A to H according to the road surface power spectral density specified in the international standard ISO-8608 [35]. This approach is widely applied in vehicle–bridge interaction studies, ensuring the comparability and comprehensiveness of the research in this paper.

Table 4. Highway maintenance quality standards.

Grade	Excellent	Good	Average	Inferior	Poor
MQI	≥90	≥80, <90	≥70, <80	≥60, <70	<90

Therefore, the B grade is selected as the most unfavorable road surface grade in this paper. The B-grade bridge deck roughness sample curve (Figure 11) is used as an example.

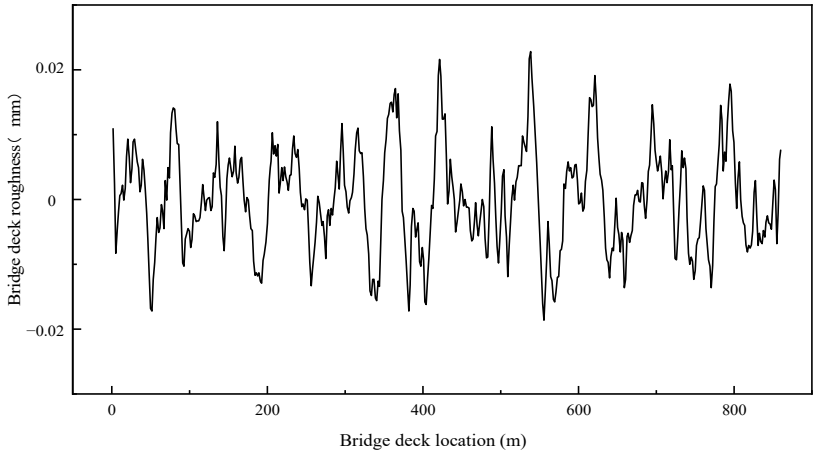

Figure 11. Class B bridge deck nonuniformity sample function.

3.5. Joint Simulation Software

A co-simulation approach combining ANSYS and Easy Language is proposed to iteratively solve the coupled vibration equations of the vehicle–bridge coupled system. ANSYS is used for the detailed modeling of the bridge and vehicle, while APDL is employed to simulate the coupled interaction relationships between the vehicle and bridge at any given time step. Easy Language is utilized to generate vehicle files, bridge surface roughness files, and macro command files for coupled analysis. The two software programs iteratively solve the coupled vibration equations. Figure 12 illustrates the co-simulation process, and the specific steps are summarized as follows:

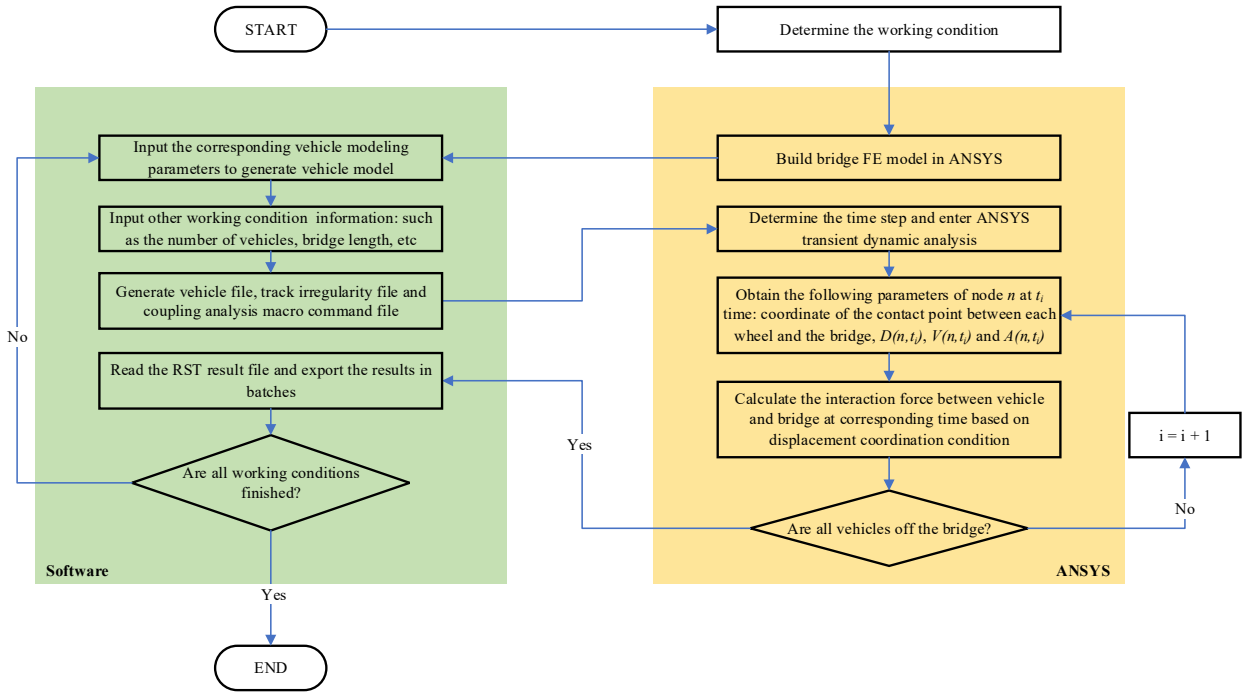

Figure 12. Joint simulation process.

Step 1: Determine the working conditions to be analyzed and build the finite element model of the bridge according to the above method.

Step 2: Input relevant calculation parameters according to the working conditions, generate vehicle files, and track irregularity files and macro command files for coupled analysis.

Step 3: Initiate the transient dynamic analysis in ANSYS and obtain the coordinates of the contact point between each wheel and the bridge, node displacement *D(n, ti)*, node velocity *V(n, ti)*, and the node acceleration *A(n, ti)* of node n at time *ti*.

Step 4: Calculate the interaction force between the vehicle and bridge at the corresponding time on the basis of the displacement coordination condition.

Step 5: Determine whether all vehicles are off the bridge or not. If so, proceed to the next step. If not, set $i = i + 1$ and repeat the process from Step 3.

Step 6: Read the RST result file and export the results. Then, check if all operations are finished and repeat the process from Step 2 if appropriate.

The combination of ANSYS and Easy Language significantly enhances computational efficiency while simultaneously advancing the automation of vehicle–bridge coupled analysis. ANSYS is used to calculate the dynamic response of bridge components when vehicles cross the bridge, and the dynamic characteristics of the structure can be accurately obtained. Self-written software can be used to quickly implement operations and generate command flows. This automates the process of vehicle–bridge coupled analysis and avoids unnecessary time wastage caused by frequent changes to the bridge model. In addition, the

response results are exported in batches with these software types for subsequent analysis. In this work, a beam arch combined system bridge is selected as an example. However, the analysis of other models can be performed via a similar process.

4. Analysis of the Vehicle–Bridge Coupled Response for Different Lane Numbers

4.1. Selection of Control Sections

For the beam–arch composite bridge, the main beam and the main arch are the main load-bearing components, and their vibration response is obvious. The boom is the connecting link between the main beam and the main arch and is affected by the joint vibration of the main beam and the main arch. The force form is clear, and the effect is prominent. In addition, the bridge piers of the project are relatively high, and the vertical stiffness is relatively weak. Combined with the natural vibration mode of the bridge, the vertical vibration of the piers is obvious.

In summary, the mid-span section of the main beam of each span, the highest point of the main arch top, the anchorage area of the boom, and the section at the top of the pier are selected for further analysis. Many studies have shown that the dynamic responses of short booms in arch bridges are more prominent than those of long booms. Therefore, the shortest boom in each span is selected for calculation and analysis. After the cross-sectional position is determined, the response time history curve for each span is calculated for a two-axle car traveling at 70 km/h on lane #1 of a B-grade road, as shown in Figure 13.

The main beam bending moment, displacement, and arch displacement all peak at span #4; the pier top bending moment increases from the bridge entry side to the bridge exit side, reaching an extreme value at pier #16; and the pier top displacement of pier #16 is the largest. The short hanger tension gradually increases in the driving direction, reaching the maximum value at span #5. In summary, the control section and other features are selected as shown in Table 3, and the typical effects in the subsequent analysis are combined.

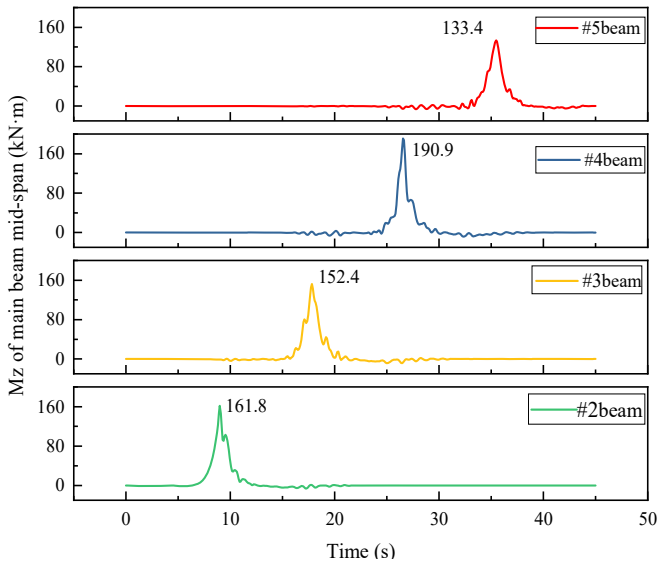

(**a**) *Mz* of the main beam mid-span

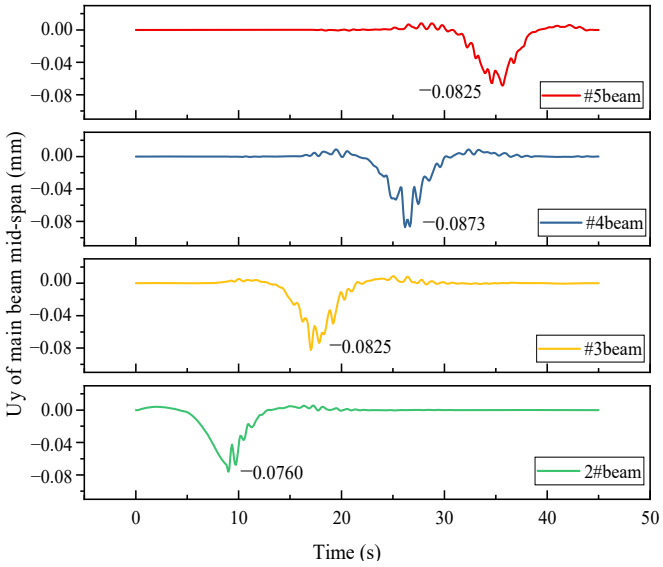

(**b**) *Uy* of the main beam mid-span

Figure 13. *Cont.*

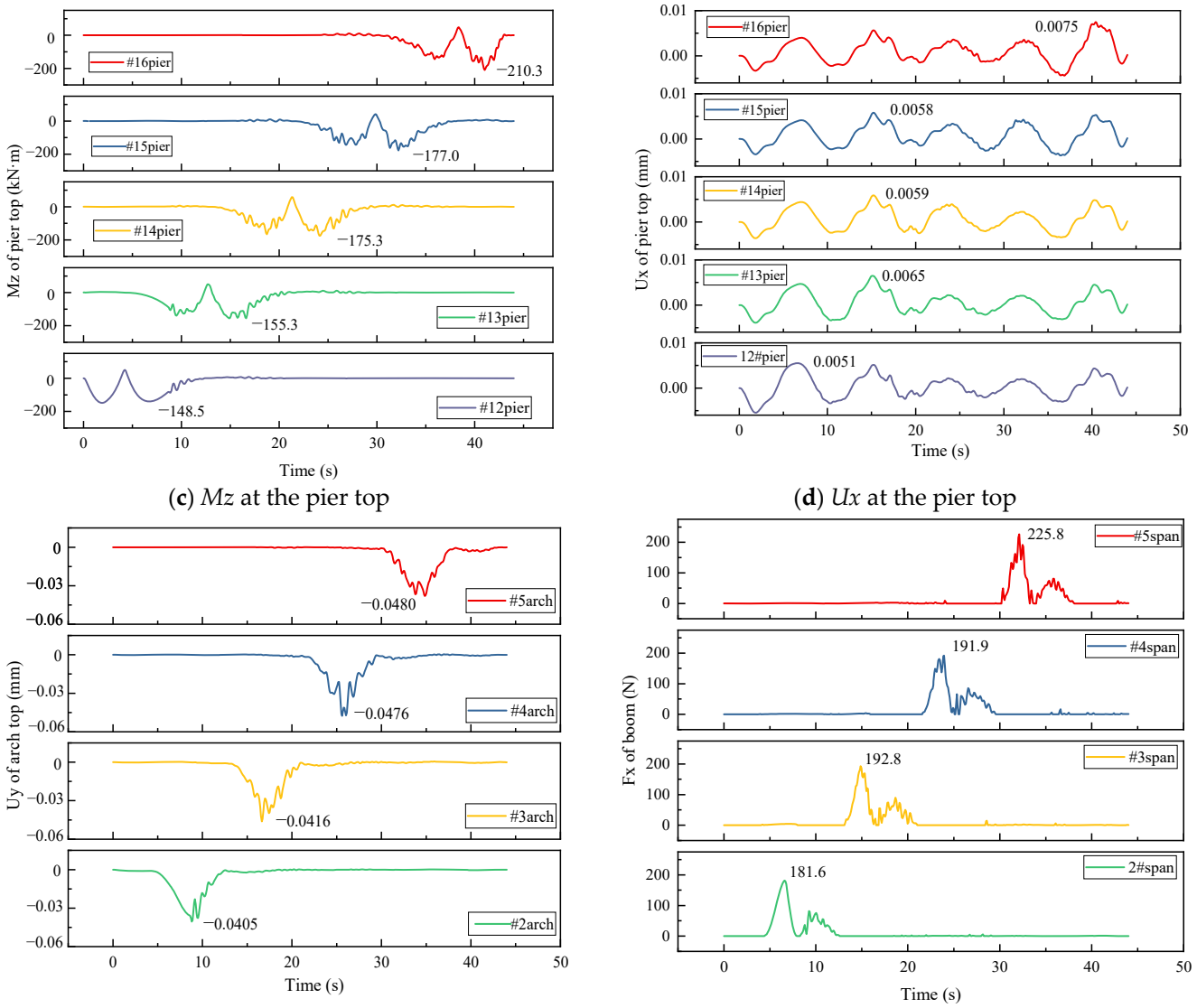

(**c**) *Mz* at the pier top

(**d**) *Ux* at the pier top

(**e**) *Uy* at the arch top

(**f**) *Fx* for the boom

Figure 13. Response time history curves.

The locations of control features listed in Table 5 are shown in Figure 14.

Table 5. Control section and features.

Section	Location	Calculation Content	Control Features
Mid-span section #4	G3-3	Mz, Uy	G3-3-Mz, G3-3-Uy
Pier top section #16	P5-5	Mz, Ux	P5-5-Mz, P5-5-Ux
Span arch section #4	A3-3	Uy	A3-3-Uy
Short span boom #5	#5	Fx	#5-Fx

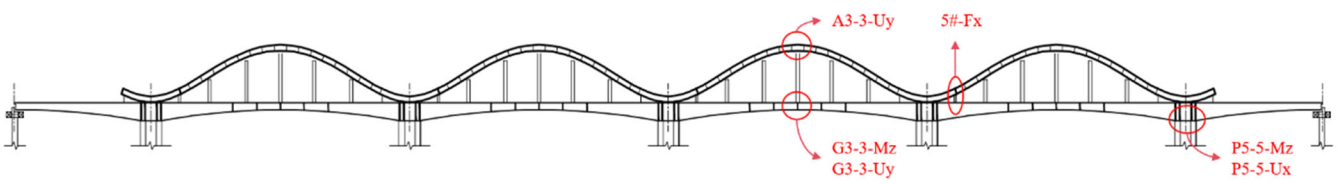

Figure 14. Locations of control features.

4.2. Selection of Working Conditions

A change in the number of vehicles in the single-lane case affects the dynamic response of the bridge, and calculations show that when a two-axle car travels at 60 km/h, a single lane can bear a maximum of 14 vehicles (fully occupying the bridge). Therefore, the DAF of the typical effect of the control section is calculated for 1–14 two-axle cars traveling in a single lane.

As shown in Figure 15, as the number of vehicles changes, the DAF increases when there are 1 and 11 vehicles. In actual traffic flows, it is not common for 11 vehicles to travel in a dense formation in a single lane; thus, in the calculation, there is 1 vehicle traveling in each lane.

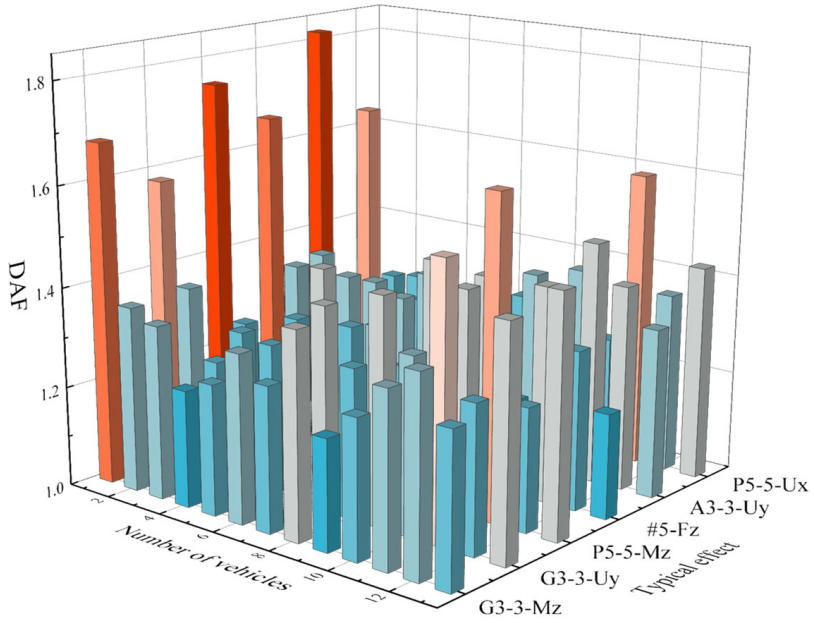

Figure 15. Comparison of the DAFs for different numbers of vehicles.

With respect to speed selection, different models have different sensitivities to speed. The operating speeds of two-axle cars (2.24 t) and two-axle trucks (27.70 t) range from 60 to 120 km/h, with a step size of 10 km/h. Three-axle trucks (33.00 t) are heavier and have a lower driving speed, with an operating speed of 60–100 km/h and a step size of 10 km/h. Among the components of the beam–arch combination system, the main load-bearing components are the main beam and the main arch, so the DAFs of G3-3-Mz, G3-3-Uy, and A3-3-Uy are calculated.

The larger the DAF of a bridge is, the more prominent its dynamic response and the smaller its safety margin. Therefore, the speed associated with the maximum DAF is selected as the most unfavorable speed. As shown in Figure 16, the most unfavorable speed is 70 km/h for a two-axle car, 90 km/h for a two-axle truck, and 60 km/h for a three-axle truck. Each vehicle type and its most unfavorable speed are combined in cases with single-lane conditions, dual-lane conditions, and three-lane conditions, as shown in Figure 17. The #1, #2, and #3 lanes are 1.875, 3.625, and 5.375 m away from the centerline of the bridge, respectively.

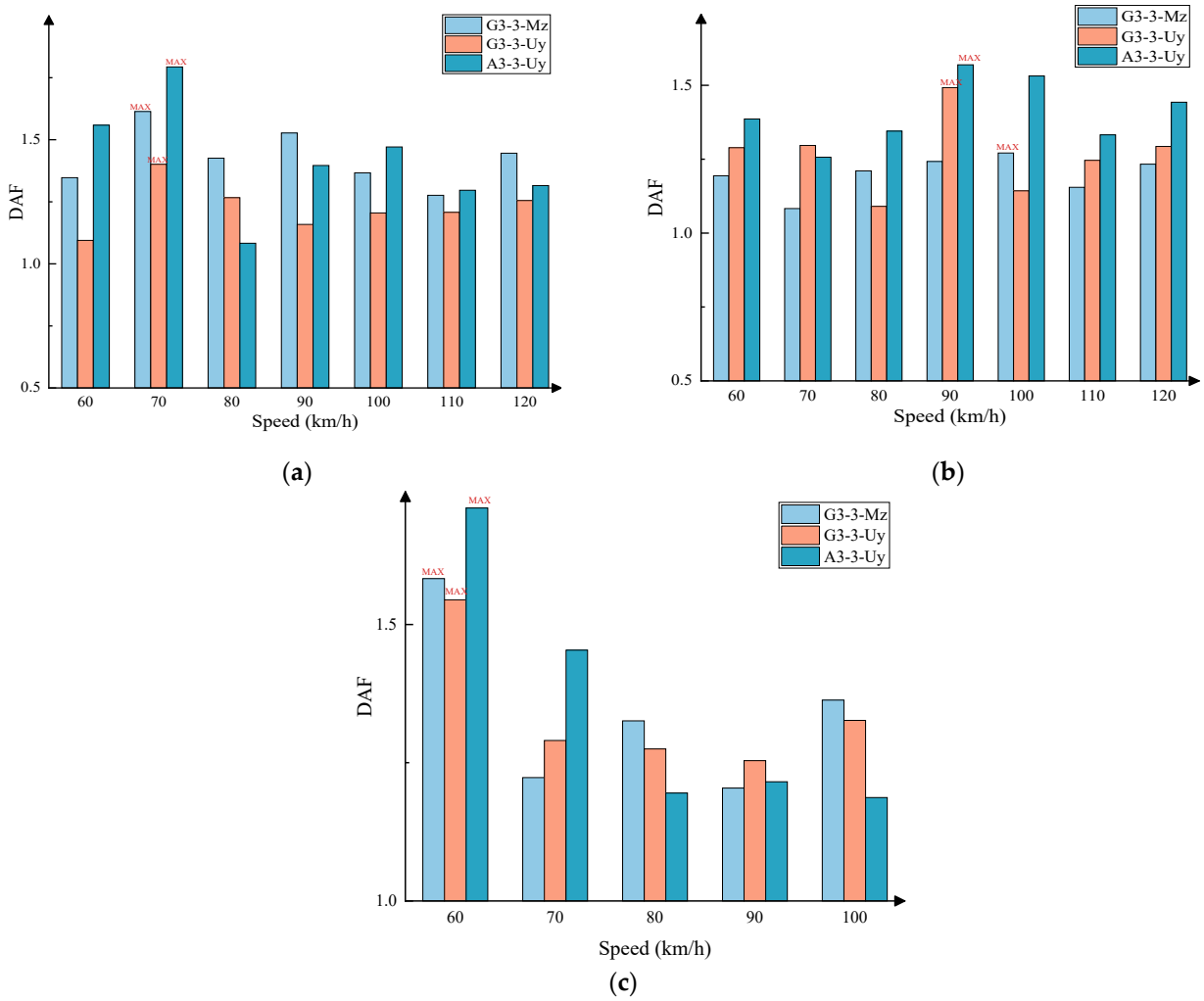

Figure 16. Comparison of the DAF for different vehicle types and speeds: (**a**) DAF of a two-axle car; (**b**) DAF of a two-axle truck; (**c**) DAF of a three-axle truck.

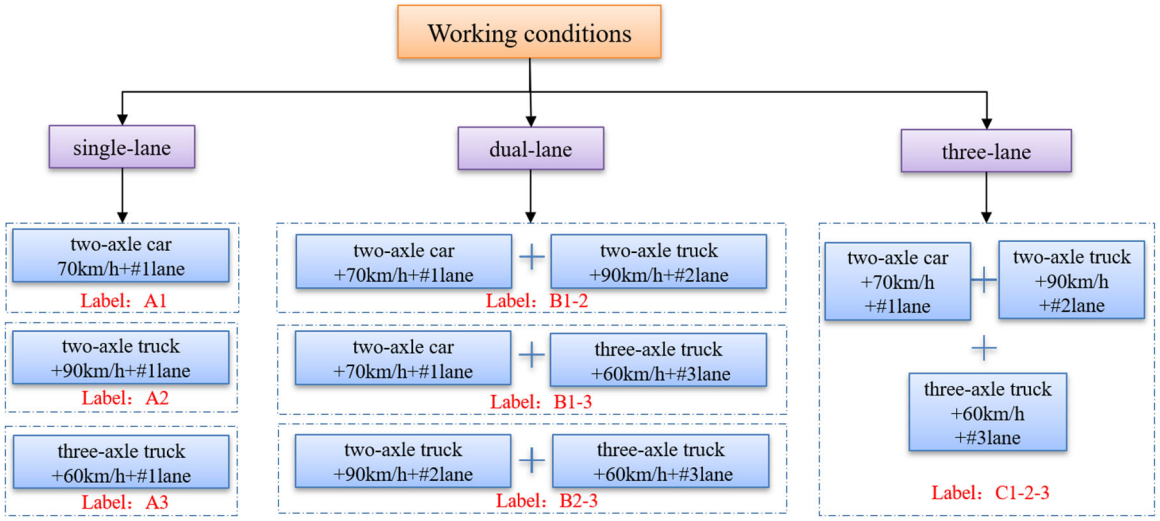

Figure 17. Working conditions.

4.3. Analysis of the Dynamic Response According to the Number of Lanes

The dynamic response of the bridge is calculated via the vehicle–bridge coupled vibration response analysis system. In the analysis, the dynamic responses under different

working conditions are sorted, the maximum dynamic response is selected as the baseline value, and the ratio of the response value to the baseline value is calculated for normalization. For example, the reference value of G3-3-Mz is 2754 kN·m for the A3 working condition, as shown in Table 6.

Table 6. G3-3-Mz comparison.

Working Conditions	A1	A2	A3	B1-2	B1-3	B2-3
Mz (kN·m)	171	2158	2754	1991	2412	2419
Ratio	0.062	0.784	1.000	0.723	0.876	0.878

The typical effect–dynamic response ratio for the sections with physical control is shown in Figure 18.

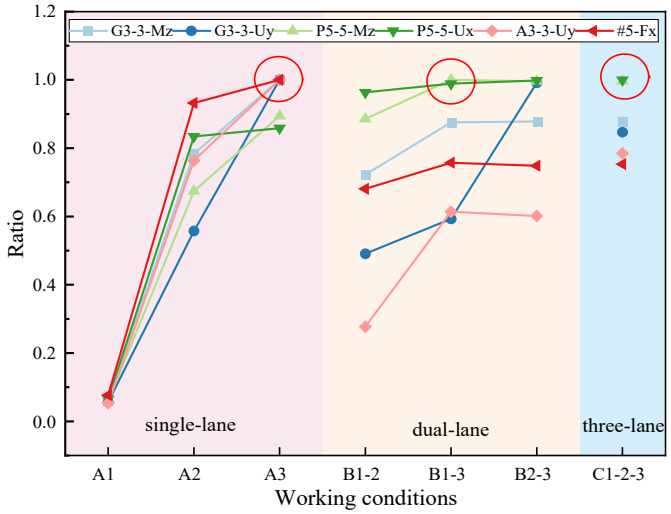

Figure 18. Comparison of the dynamic responses.

First, we focus on the baseline values of the typical effects of each control section. The baseline values of G3-3-Mz, G3-3-Uy, A3-3-Uy, and #5-Fx were all obtained under the A3 condition (Figure 19). Studies have shown that vehicles traveling in a single lane are more likely to cause resonance between the bridge and the vehicle than are evenly distributed vehicles traveling in multiple lanes.

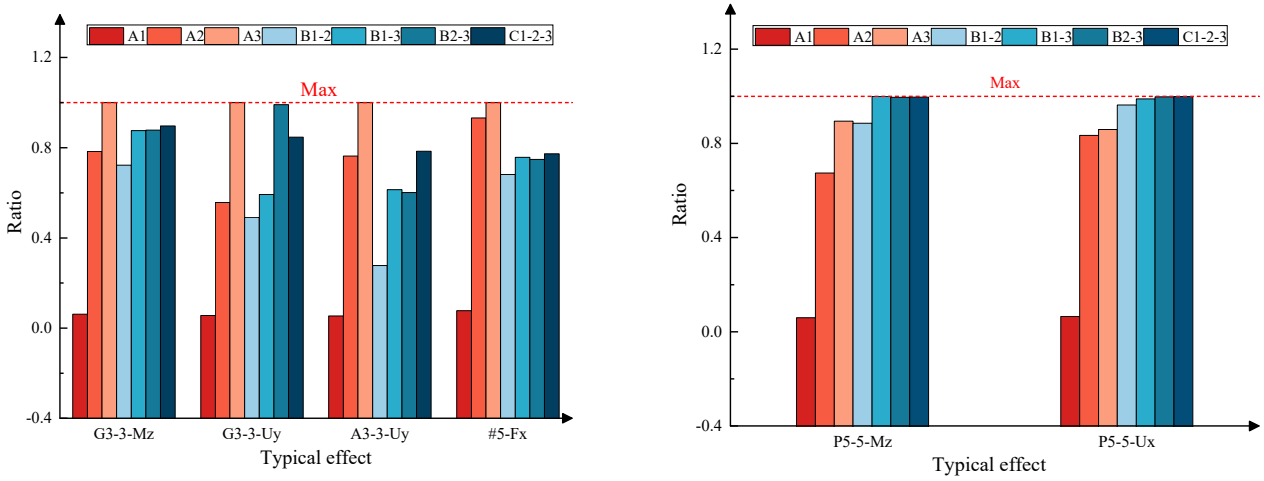

Figure 19. Dynamic response comparison.

According to the vehicle resonance criterion based on the frequency response function (FRF) [36]:

$$\omega_u = \sqrt{\frac{k_j(d_1 + d_2)}{M_v d_i}} (i \neq jandi, j = 1, 2)$$

While the excitation frequency approaches the bridge's natural frequency, taking the first mode as an example, the overall natural frequency of 0.23786 Hz is less than 1.5 Hz, whereas according to the literature, the calculation for two-axle vehicles is 2.78 Hz or 2.50 Hz. As vehicle weight increases, its frequency gradually approaches the bridge's natural frequency, thereby triggering resonance.

Therefore, the A3 condition is suspected to be associated with vehicle–bridge resonance since the dynamic response of the bridge surges and the benchmark value is concentrated in a certain region. The baseline values of P5-5-Mz and P5-5-Ux are obtained under the B1-3 and B2-3 conditions, respectively, and the dynamic responses of these two effects under the B1-3, B2-3, and C1-2-3 conditions are basically the same, with ratios of 0.989 to 0.998 in relation to the baseline values. The pier, as the lower structural component, is less affected by resonance, and the dynamic response is affected mainly by the vehicle weight. Bridge piers, as substructures, are less affected by resonance because of their higher natural frequencies, which respond primarily to vehicle weight. Additionally, their connection to the foundation provides damping effects, reducing sensitivity to resonance and high-frequency vibrations. Under multilane conditions, there are many vehicles, and the vehicles are heavy, so the pier top effect is prominent.

For single-lane conditions, the dynamic response reaches a minimum under the A1 condition, increases under the *A*2 condition, and reaches a maximum under the A3 condition (Figure 20), with a maximum increase of 17.66 times the base value. The reason is that the weights of a two-axle car, two-axle truck, and three-axle truck are 2.24 t, 27.70 t, and 30.50 t, respectively, and A1 < A2 < A3 is related to the vehicle weight. As the weight of the moving vehicle increases, the possibility of resonance increases, and the dynamic responses of the main load-bearing components increase. That is, when driving in a single lane, the heavier the vehicle is, the more obvious the vibration of the bridge and the more prominent the dynamic response of the typical effect of the control section.

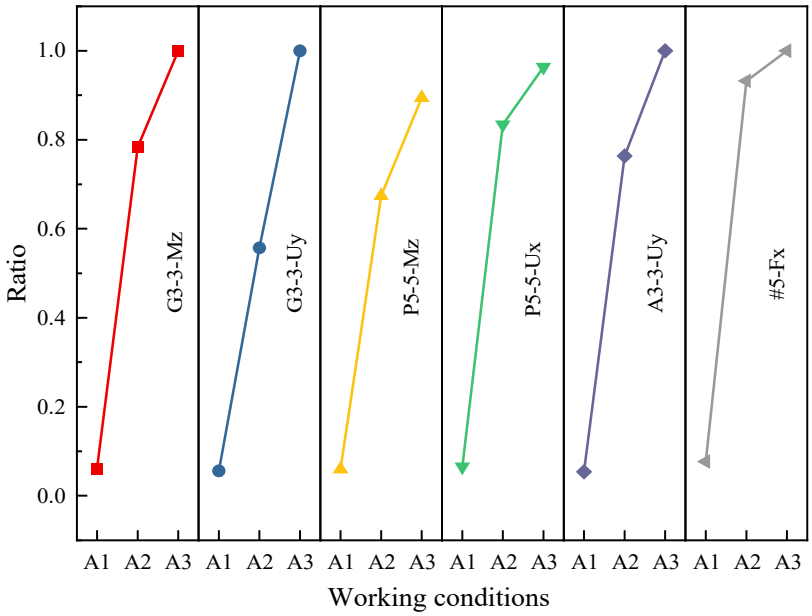

Figure 20. Comparison of the dynamic responses under single-lane conditions.

For the dual-lane conditions, all the effects show the minimum dynamic response under the B1-2 condition and the maximum dynamic response under the B2-3 condition (Figure 21); the maximum increase is 1.21 times the base value, and the minimum increase is 11.2%. Compared with that under other dual-lane conditions, the vehicle weight for B1-2 is the smallest, and the driving position is closest to the centerline of the bridge, with the smallest eccentricity. The greater the eccentricity associated with the driving position is, the more prominent the dynamic response.

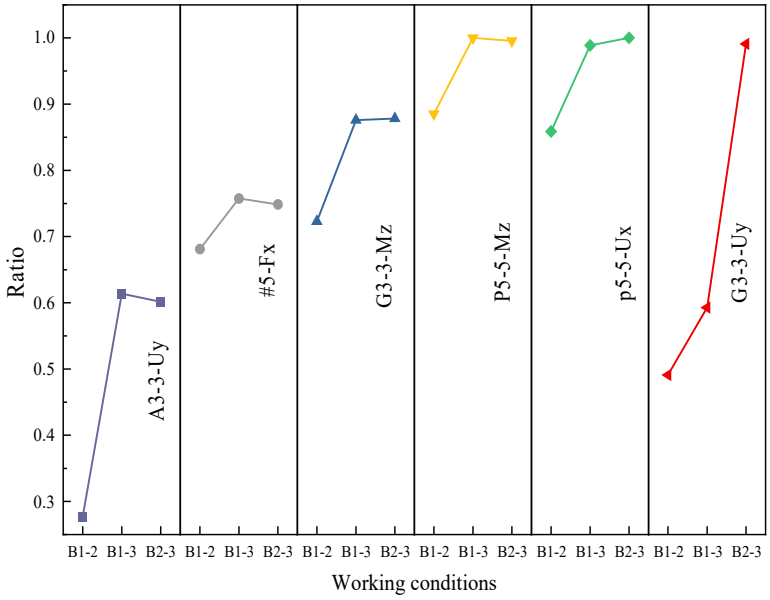

Figure 21. Dynamic response comparison under dual-lane conditions.

Both the B2-3 and C1-2-3 conditions include multiple heavy vehicles. Compared with those under the B2-3 condition, the vehicle weights under the C1-2-3 condition are greater, and the eccentricity is lower, but those under the G3-3-Mz, P5-5-Mz, P5-5-Ux, #5-Fx, and A3-3-Uy conditions are the same or increase, with the smallest growth rate being 0.18% and the largest being 30.5%.

When the vehicle loading position changes from lane #2 to lane #3, the bridge dynamic response increases significantly, with G3-3-Uy and G3-3-Mz increasing by 20.7% and 21.1% respectively, and A3-3-Uy increasing by 1.213 times. Considering that changes in vehicle lateral loading position will cause changes in bridge bending and torsional moments, we calculated both separately. Under condition B1-2, a two-axle truck (27.70 t) in lane #2 produces a torsional moment of approximately 986.06 kN·m, a main girder bending moment of 17,527.8 kN·m, and a main arch bending moment of 689.55 kN·m. Under condition B1-3, a three-axle truck (33.00 t) in lane #3 produces a torsional moment of approximately 1740.05 kN·m, a main girder bending moment of 20,880.8 kN·m, and a main arch bending moment of 1218.03 kN·m, representing increases of 76.64%, 19.13%, and 76.64% respectively.

When vehicles move from the center position to the side lanes, the dynamic response of the bridge increases nonlinearly, far exceeding the impact brought by increased vehicle weight. This is mainly due to the increased eccentric distance causing significant bending–torsion coupling effects. Analysis shows that eccentric loads not only produce main girder bending moments but also cause overall structural torsion and out-of-plane deformation of arch ribs, which together produce an amplification effect. This phenomenon reveals that in long-span beam-arch composite bridges, the coupling mechanism between torsional and bending effects may lead to structural stability issues. In practical engineering, analysis of eccentric load conditions should be strengthened, lateral structural connections enhanced,

cross-section design optimized, and if necessary, lane management measures implemented to prevent safety risks and performance degradation caused by excessive amplification of dynamic response.

In summary, vehicle–bridge resonance is suspected to occur under single-lane conditions, the bridge vibrations and dynamic responses are more obvious than those under multilane conditions, and the dynamic responses under dual-lane and three-lane conditions remain essentially stable. Under single-lane conditions, vehicles are concentrated at a specific location on the bridge, leading to significant localized dynamic responses, and the absolute value of the excitation frequency generated by the vehicles is relatively large. Under multilane conditions, the vibration frequencies generated by different vehicles tend to cancel each other out, resulting in smaller absolute values of the vehicle excitation frequency. Therefore, under single-lane conditions, the probability of the bridge's natural frequency coinciding with the vehicle excitation frequency is higher than that under other conditions, and this frequency matching increases the likelihood of vehicle–bridge resonance.

The main factors affecting the dynamic response of the beam–arch composite bridge are the vehicle weight and eccentricity. According to the analysis results, when driving on a single-lane road, the greater the vehicle weight is, the greater the vibration and dynamic response of the bridge. When driving on a multiple-lane road, when the vehicle weight is low, eccentricity is the main influencing factor, and the greater the eccentricity is, the greater the vibration and dynamic response of the bridge. When the vehicle weight is large, the vehicle weight is the main influencing factor, and the greater the vehicle weight is, the greater the bridge vibration and the more obvious the dynamic response. Under multilane conditions, owing to the eccentricity effect of vehicle loads, larger eccentricities lead to more pronounced torsional effects on the bridge, resulting in greater dynamic responses. Moreover, the influence of vehicle weight means that heavier vehicles induce larger dynamic responses. However, the interaction between multiple vehicles in multilane conditions can suppress the overall dynamic response. The combined effect of multiple vehicles reduces the risk of resonance and distributes the moving load more evenly across the bridge [37].

4.4. Analysis of the DAF According to the Number of Lane Changes

The static and dynamic responses of the bridge under various working conditions are calculated, the static and dynamic responses of the typical effects of the control section are extracted in Section 3.1, and the DAF is calculated according to Equation (12).

When the number of lanes was varied, different trends regarding the DAF were observed (Figure 22). On the one hand, the DAFs of G3-3-Uy and A3-3-Uy displayed the trend of single-lane > three-lane > dual-lane. To consider the safety margin and the most unfavorable state of the structure, it is necessary to consider the maximum value of the DAF of each effect. The maximum DAF of G3-3-Uy under single-lane conditions is 1.78, that under dual-lane conditions is 1.47, and that under three-lane conditions is 1.43, with reductions of 6.2% and 14.4%, respectively. Similarly, the reductions for A3-3-Uy were 16.7% and 4.0%, respectively. On the other hand, the DAFs of G3-3-Mz and #5-Fx decreased in the order of single-lane > dual-lane = three-lane. The maximum DAF for the single-lane G3-3-Mz case was 1.29, and the DAF for the dual-lane and three-lane G3-3-Mz cases fluctuated by approximately 1.24. The DAF reduction was 4.0%. Similarly, the DAF reduction for #5-Fx was 6.7%. In addition, the DAFs of P5-5-Mz and P5-5-Ux decreased in the order of single-lane < dual-lane = three-lane. The maximum DAF of P5-5-Mz increased from 1.062 to 1.064, with a growth rate of 0.18%, and the growth rate for P5-5-Ux was 1.2%. By comparison, the DAFs of the main beam, main arch, and suspender are all greater for the single-lane case than for the multiple-lane cases, and the reduction rate is between

4.0% and 16.7%. For the main pier, the DAF under single-lane conditions is less than that under multiple-lane conditions, and the growth rate is approximately 1.0%. The DAFs for dual-lane and three-lane working conditions remain essentially stable, with fluctuations within 10%.

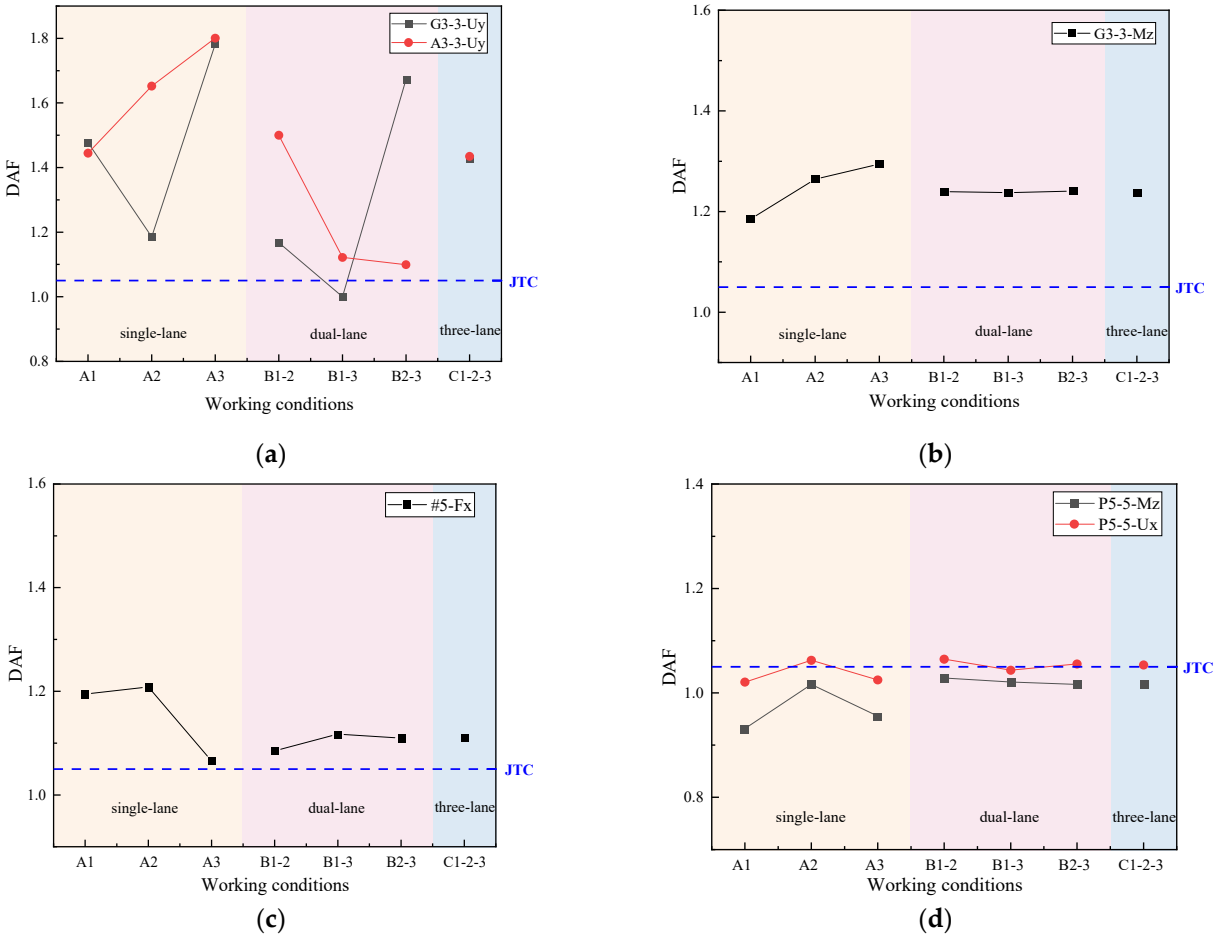

Figure 22. Comparison of DAFs: (**a**) comparison of the DAFs of G3-3-Uy and A3-3-Uy; (**b**) comparison of the DAFs of G3-3-Mz; (**c**) comparison of the DAFs of #5-Fx; and (**d**) comparison of the DAFs of P5-5-Mz and P5-5-Ux.

The maximum DAF values of P5-5-Mz and #5-Fx are less than 1.05, which is in line with the relevant specification. The DAF values in other cases all exceeded 1.05. The actual calculated impact coefficient can reach up to 16 times the value recommended by the specification (Table 7). The high impact coefficient is manifested as the dynamic response and amplitude caused by the structural vibration exceeding the designed safety value, which poses a safety hazard during the operation and use stages.

Table 7. Impact coefficient comparison.

Member	Main Beam	Main Arch	Boom	Main Pier
JTC impact factor		0.05		
Calculated impact factor	0.78	0.80	0.21	0.09
Recommended impact factor	0.43	0.26	0.20	0.05

For the main load-bearing components of the beam–arch composite bridge, under single-lane conditions, the impact coefficient of the main arch is the largest, that of the main beam is the second largest, and those of the boom and the main pier are the smallest. Under

multilane conditions, the main beam has the largest impact coefficient, that of the main arch is the second largest, and those of the boom and the main pier are the smallest. Therefore, the calculation of the impact coefficient should consider the differences among components, and different impact coefficient values should be used for different components. The recommended value of the impact coefficient is based on the principle of ensuring that most of the dynamically amplified parts of the components are safe.

Separate impact coefficients should be applied to different bridge components in design and maintenance to prioritize inspections and allocate resources efficiently. Traffic regulations can be used to optimize vehicle placement by assigning heavy vehicles to inner lanes near the centerline and lighter vehicles to outer lanes, thus reducing eccentricity effects and enhancing structural safety. For autonomous vehicles, regulatory frameworks should mandate compliance with lane-specific rules on bridges to ensure safe and balanced traffic loads.

4.5. Analysis of Driving Comfort According to the Number of Lanes

The acceleration time history curve is calculated considering the vertical displacement of the driver's position, the RMS is subsequently calculated, and the driving comfort is evaluated on the basis of ISO2631.

For the single-lane condition, the acceleration time history curve in the A2 condition changes most obviously, with a maximum acceleration of 0.578 m/s^2 and the largest vehicle vibration amplitude; the acceleration time curve for the A3 condition is the least severe, with a maximum acceleration of 0.176 m/s^2 and minimal vehicle vibration (Figure 23). In the driving comfort evaluation, the RMS value of the A2 condition is the largest, at 1.42 m/s^2, and the occupants feel uncomfortable. The RMS under the A3 condition is the smallest, at 0.67 m/s^2, and the occupants feel somewhat uncomfortable. The RMS values for the three conditions displayed the order of A2 > A1 > A3, with reductions of 40% and 20% in the latter two cases, respectively. The A2 condition was associated with the highest level of comfort, followed by A1 and, lastly, *A*3. Combined with the specific layout of the three working conditions, different vehicles adopted different driving speeds A2 (90 km/h) > A1 (70 km/h) > A3 (60 km/h), the patterns of acceleration and RMS changes also followed the order of A2 > A1 > A3, and the greater the RMS was, the more uncomfortable the occupants felt. The main factor affecting driving comfort under single-lane conditions was the driving speed. The greater the speed is, the worse the driving comfort.

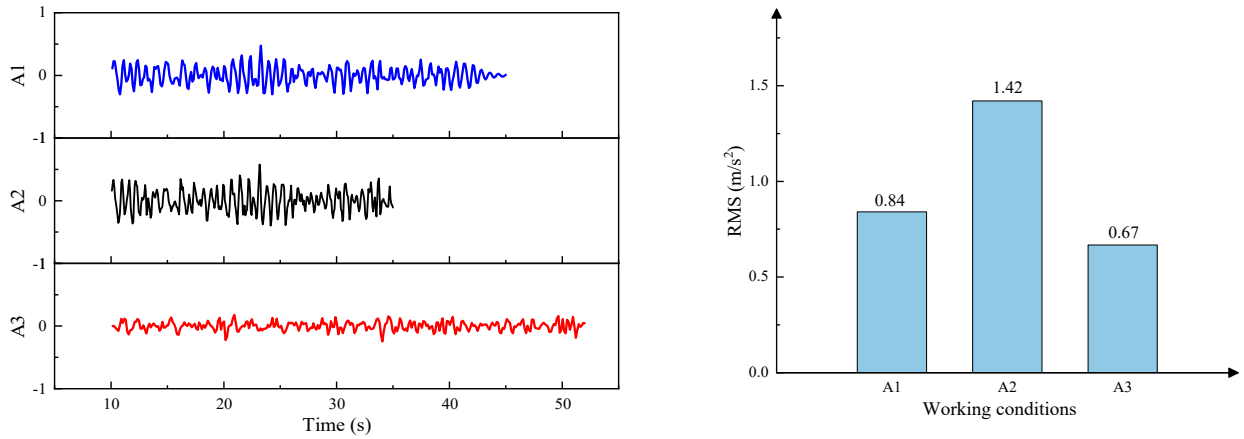

(**a**) (**b**)

Figure 23. Driving comfort evaluation for single-lane acceleration. (**a**) Single-lane acceleration time history curves; (**b**) evaluation of driving comfort I.

For dual-lane conditions, attention should be given to the changes in driving comfort in different lanes under the same conditions. As shown in Figure 24a, the acceleration of vehicles in the outer lane is always greater than that in the inner lane. For example, the maximum acceleration in inner lane 1 under the *B*1—2 condition is 0.43 m/s^2, and the maximum acceleration in outer lane 2 is 1.69 m/s^2, which is a 2.93-fold increase in acceleration. Similarly, the peak acceleration under the B1-3 condition increases by 86.8%, and the peak acceleration under the B2-3 condition increases by 70.1%; that is, the acceleration of vehicles in the outer lane changes considerably, and the vehicle vibration is obvious. As shown in Figure 24b, the RMS value at the driver's position in the outer lane is always greater than that in the inner lane. For example, the RMS in inner lane 1 under the B1-2 condition is 0.98 m/s^2, which is classified as uncomfortable, and the RMS in outer *lane* #2 is 3.19 m/s^2 (an increase of 2.25 times), which is classified as extremely uncomfortable. Similarly, the RMS under the B1-3 condition increases by 89%, and the RMS under the B23 condition increases by 1.11 times. This is because when the vehicle is traveling in the outer lane, the eccentricity is high, resulting in a larger dynamic bridge response, an increase in vehicle vibration in the bridge system, increases in the acceleration and RMS, and a reduction in driving comfort.

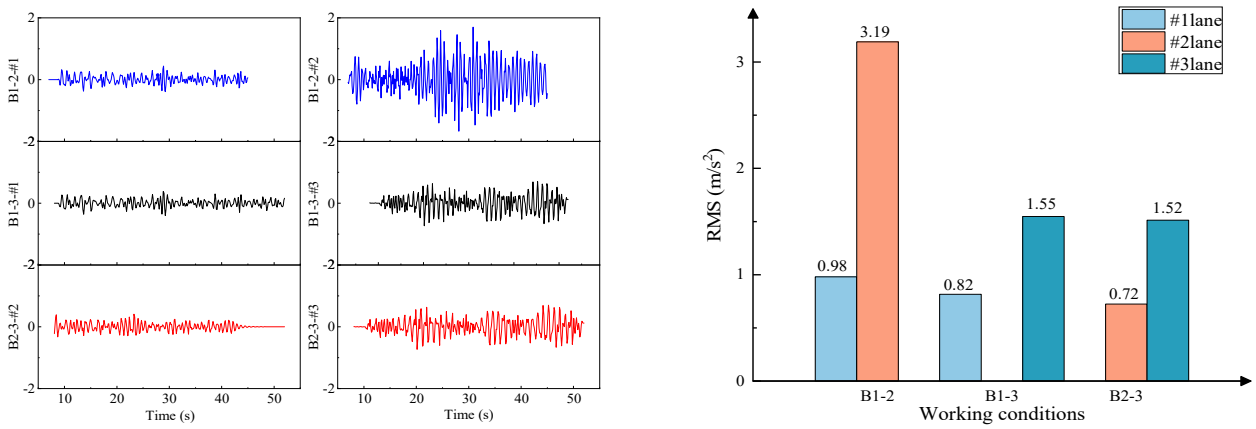

(**a**) (**b**)

Figure 24. Driving comfort evaluation for dual-lane acceleration. (**a**) Dual-lane acceleration time history curves; (**b**) evaluation of driving comfort II.

For the C1-2-3 condition, the acceleration for lane #2 changes significantly, with a maximum acceleration of 1.53 m/s^2. The acceleration for lane #1 changes the least, with a maximum acceleration of only 0.44 m/s^2 (Figure 25a). The RMS trend is the same as that of the acceleration, that is, lane #2 (3.60 m/s^2) > lane #3 (1.92 m/s^2) > lane #1 (0.90 m/s^2), whereas the driving comfort in lane #2 is described as extremely uncomfortable, and the driving comfort in lane #1 is described as somewhat uncomfortable (Figure 25b). The main factors affecting driving comfort are vehicle speed and lane position. Under the same driving conditions, the acceleration and RMS values of lane #2 are much greater than those of the other lanes, and the larger eccentricity of lane #3 does not cause a major increase in acceleration or RMS, although increases do occur. Therefore, when multiple vehicles are running in parallel, both vehicle speed and eccentricity affect driving comfort, but vehicle speed is the main factor; the higher the vehicle speed is, the lower the level of passenger comfort.

When the number of lanes is varied, the passenger comfort level changes depending on the driving method. As shown in Figure 26, the driving comfort level under single-lane conditions is best, and the passengers in the car feel relatively comfortable. The comfort level under multilane conditions is affected by the eccentricity and vehicle speed; notably, the

three-axle truck traveling in the outermost lane #3 has the largest eccentricity and an RMS value between 1.55 and 2.00 m/s^2, and the passengers in the vehicle feel very uncomfortable. The two-axle truck in lane #2 displays the highest speed and a surge in RMS value, with an average of 2.50 m/s^2, which is much greater than that of the other vehicles in other cases, and the driving comfort level is classified as extremely uncomfortable. In summary, the driving comfort level is best when driving on a single-lane road and poor when driving on a multiple-lane road. When vehicles drive on the bridge under the working conditions considered in this study, 83% of the vehicles are rated as comfortable or somewhat comfortable, and the higher the speed and eccentricity are, the worse the driving comfort level.

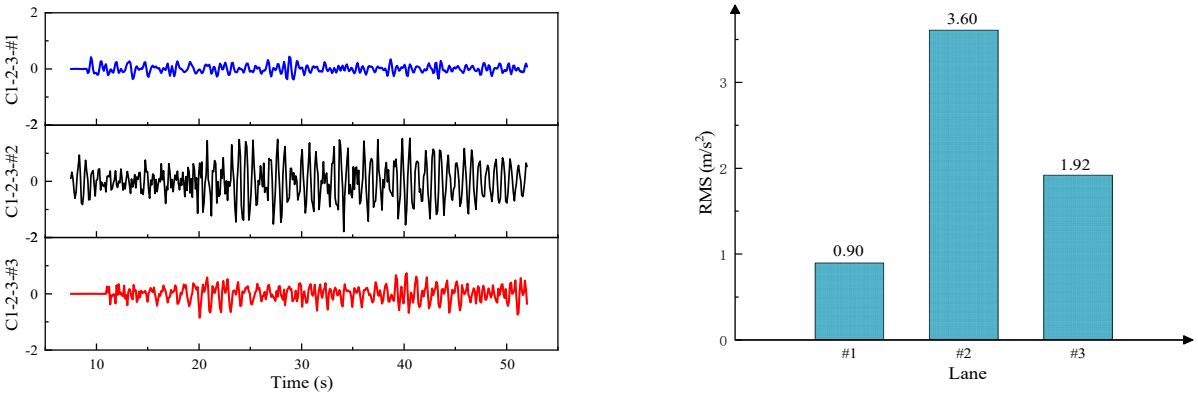

Figure 25. Driving comfort evaluation for three-lane acceleration. (**a**) Three-lane acceleration time history curves; (**b**) evaluation of driving comfort III.

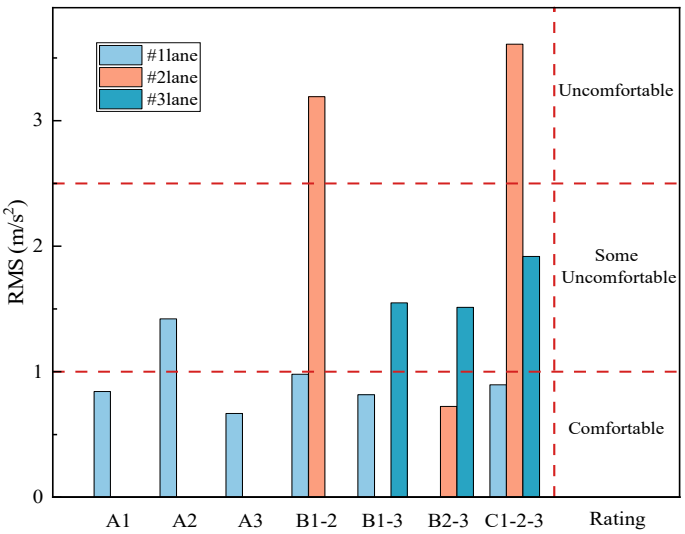

Figure 26. Driving comfort evaluation of the PC beam–steel box arch composite bridge.

Under single-lane conditions, the vehicle load is concentrated at a specific location on the bridge, resulting in significant localized vibrations. As the vehicle speed increases, the probability of the excitation frequency matching the bridge's natural frequency also increases, with increased risk of resonance, which amplifies vibration levels and reduces comfort. Dynamically adjusting vehicle speed can be an effective approach, reducing speed when bridge conditions and road surfaces are poor to minimize dynamic loads and improve driving comfort, while appropriately increasing speed when conditions permit to optimize throughput. Under multilane conditions, the presence of multiple vehicles distributes the load and reduces localized vibrations. Additionally, the interaction between

vehicles suppresses the overall bridge vibration, thereby mitigating the impact of increased vehicle speed on comfort. The research results provide insights for bridge design and traffic management. Driving comfort can be improved by considering the lane configuration and avoiding multiple vehicles driving at high speeds in the outer lane.

Compared with manually driven vehicles, autonomous vehicles can accelerate, decelerate, and change lanes more smoothly. This driving style reduces sudden jolts and abrupt stops, thereby improving ride comfort. Using advanced sensors and algorithms, autonomous vehicles can predict and adapt to road conditions, optimize speed and driving trajectories to minimize the impact of road heterogeneities, reduce bridge vibrations and resonance effects, and maintain a high level of passenger comfort. However, in the early stages of autonomous driving systems, inaccuracies in interpreting complex traffic scenarios may lead to sudden braking or steering adjustments, reducing ride comfort. Additionally, the conservative decision-making of autonomous systems (e.g., frequent braking or slow lane changes) may cause discomfort for passengers. Through the coupled vehicle–bridge calculations and analysis in this paper, comfort indicators can be identified for use in the design of autonomous vehicles integrated with real-time monitoring systems to enhance consideration of passenger ride comfort in the decision-making process of autonomous driving. By improving algorithms, smooth transitions in acceleration, braking, and lane changes can be ensured.

5. Conclusions

In this work, a vehicle–bridge coupled dynamic model of a spatial multi-degree-of-freedom, in-wheel-driven electric vehicle–PC beam–steel box arch composite system was established. The vehicle–bridge coupled motion equation was derived and solved iteratively via the Newmark-β method. The dynamic response and dynamic amplification factor (DAF) of the bridge with various loading conditions and numbers of lanes were analyzed, and the driving comfort level was evaluated according to ISO2631. The main conclusions are as follows:

(1) Dynamic response: Under single-lane conditions, the bridge exhibited the largest dynamic response when a heavy vehicle was driving on the bridge, with vehicle weight being the main influencing factor. The dynamic response increased by up to 17.66 times as the vehicle weight increased.

Under multilane conditions, eccentricity was the main factor when the vehicle weight was low, with greater eccentricity leading to greater dynamic responses. When the vehicle weight was high, it became the dominant factor.

(2) Dynamic amplification factor (DAF): The DAF of the main beam, main arch, and boom was greater under single-lane conditions than under multilane conditions, with a reduction of 4.0–16.7%. Under dual-lane and three-lane conditions, the DAF remained relatively stable, with fluctuations within 10%.

(3) Driving comfort: Driving comfort decreased as the number of traffic lanes increased. Under single-lane conditions, the vehicle speed was the main influencing factor. Under multilane conditions, driving comfort was affected by vehicle speed and eccentricity, with speed being the dominant factor.

(4) Impact coefficient: The calculated impact coefficient significantly exceeded the code-recommended values, and the impact coefficients of different system components varied. It is recommended that separate impact coefficients be set for each component to guide the design and maintenance of bridges, set speed limits, and optimize driving positions.

This study provides a comprehensive framework for analyzing vehicle–bridge coupled vibration and driving comfort levels in beam–arch composite systems. The theoretical model of vehicle–bridge coupling for the beam–arch composite system established in this

paper has good applicability and scalability. Future research could explore the following topics. In subsequent research, by modifying key parameters such as bridge parameters (span, rise-to-span ratio, hanger spacing, etc.) and vehicle parameters (vehicle type, lane change, acceleration and deceleration, etc.), the model can be extended to other beam–arch composite bridge systems for parametric variation analysis. This would enable comprehensive investigation of how different bridge design configurations and traffic flows affect vehicle–bridge coupling vibrations, facilitate exploration of the relationship between bridge design and driving comfort, establish a more universally applicable impact factor prediction model for beam–arch composite systems, provide impact factor recommendations that better match actual working conditions, and offer bridge operation and design methods with driving comfort as a controlling factor.

Author Contributions: Conceptualization, H.S.; methodology, W.L.; validation, Y.L.; formal analysis, H.S.; investigation, X.L.; resources, X.L. and Y.L.; data curation, K.C.; writing—original draft preparation, W.L.; visualization, L.W.; supervision, X.L. and Y.L.; project administration, L.W. and K.C. All authors have read and agreed to the published version of the manuscript.

Funding: This research was funded by the National Key Research and Development Program of China (Grant No. 2021YFB1600305); Natural Science Basic Research Program of Shaanxi (Program No. 2022JC-23); and Science and Technology Project of the Department of Transport of Shaanxi Province (Grant No. 21-63K).

Data Availability Statement: The datasets generated during and/or analyzed during the current study are available from the corresponding author upon reasonable request.

Conflicts of Interest: Author Xiaoguang Liu is employed by the SCEGC Mechanized Construction Group Co., Ltd. The remaining authors declare that the research was conducted in the absence of any commercial or financial relationships that could be construed as a potential conflict of interest.

Abbreviations

DAF dynamic amplification factor

References

1. Han, W.; Wang, T.; Li, Y.; Li, Y.; Huang, P. Vehicle-bridge coupling vibration analysis system based on model-modified grillage method. *China J. Highw. Transp.* **2011**, *24*, 47–55. [CrossRef]
2. Zhou, Z.; Wang, D.; Wang, R.; Zhang, P.; Zhang, M. Dynamic impact factor for steel-concrete composite l-girder bridge based on vehicle-bridge. *Earthq. Eng. Eng. Dyn.* **2022**, *42*, 127–137. [CrossRef]
3. Sun, R.; Wang, S.; Li, M.; Zhu, Y. An algorithm for large-span flexible bridge pose estimation and multi-keypoint vibration displacement measurement. *Measurement* **2025**, *240*, 115582. [CrossRef]
4. Gao, Q.; Zhang, K.; Wang, T.; Peng, W.; Liu, C. Numerical investigation of the dynamic responses of steel-concrete girder bridges subjected to moving vehicular loads. *Meas. Control* **2021**, *54*, 465–484. [CrossRef]
5. Zhang, C.; Li, H. Active Control for Construction Stability of Suspension Arch Rib Segments Based on ARID System. *Int. J. Struct. Stab. Dyn.* **2024**. [CrossRef]
6. Zhou, Y.; Yang, P.; Zhang, K. Dynamic response analysis of cable-stayed bridge under random traffic flow and fleet. *J. Vibroeng.* **2021**, *23*, 1663–1679. [CrossRef]
7. Guo, F.; Cai, H.; Li, H. Impact coefficient analysis on long-span beam bridge. *J. Vibroeng.* **2021**, *23*, 436–448. [CrossRef]
8. Xie, R.; Li, M.; Xu, C. Study on the Technical Status of Old Concrete Truss-Arch Bridge Based on Vehicle-Bridge Interaction. *Adv. Civ. Eng.* **2022**, *2022*, 9946957. [CrossRef]
9. Li, X.; Wang, X.; MU, B.; Yuan, Z. Research on Vibration Control of Twin-I Steel-concrete Composite Continuous Girder Bridge Under Vehicle Load. *China J. Highw. Transp.* **2022**, *35*, 173–183. [CrossRef]
10. Wang, S.; Lin, S.; Yang, R. A lightweight convolutional neural network for multipoint displacement measurements on bridge structures. *Nonlinear Dyn.* **2024**, *112*, 11745–11763. [CrossRef]
11. Zhou, Z.; Wang, Y.; Zhou, G.; Liu, X.; Wu, M.; Dai, K. Vehicle Lateral Dynamics-Inspired Hybrid Model Using Neural Network for Parameter Identification and Error Characterization. *IEEE Trans. Veh. Technol.* **2024**, *73*, 16173–16186. [CrossRef]

12. Chen, J.; Yu, C.; Wang, Y.; Zhou, Z.; Liu, Z. Hybrid modeling for vehicle lateral dynamics via AGRU with a dual-attention mechanism under limited data. *Control Eng. Pract.* **2024**, *151*, 106015. [CrossRef]
13. Liang, J.; Yang, K.; Tan, C.; Wang, J.; Yin, G. Enhancing High-Speed Cruising Performance of Autonomous Vehicles Through Integrated Deep Reinforcement Learning Framework. *IEEE Trans. Intell. Transp. Syst.* **2025**, *26*, 835–848. [CrossRef]
14. Zhang, Y.; Li, W.; Ji, Z.; Wang, G. Vehicle Ride Comfort Analysis Based on Vehicle-Bridge Coupled Vibration. *Shock Vib.* **2021**, *2021*, 5285494. [CrossRef]
15. Gao, Q.; Wang, Z.; Chen, C.; Guo, B. Comfort Analysis of Large-Span Continuous Girder Bridges to Moving Vehicular Loads. *Key Eng. Mater.* **2014**, *3322*, 61–70. [CrossRef]
16. Kirbas, U. Determination of ride comfort thresholds based on international roughness index for asphalt concrete pavements. *Int. J. Pavement Eng.* **2023**, *24*, 2011279. [CrossRef]
17. Li, Z.; Wang, X.; Ding, Y.; Wang, J.; Liu, P.; Deng, Z. Study on the Dynamics Characteristics of HTS Maglev Train Considering the Aerodynamic Loads under Crosswinds. *Sustainability* **2023**, *15*, 16511. [CrossRef]
18. Zhang, G.; Xu, Y.; Wang, B.; Zhu, Q. Turbulence Effects on Vortex-Induced Dynamic Response of a Twin-Box Bridge and Ride Comfort of the Vehicle. *Int. J. Struct. Stab. Dyn.* **2023**, *23*, 2340023. [CrossRef]
19. Zhang, G.; Wang, B.; Zhu, Q.; Xu, Y. Dynamic behavior and ride comfort of a vehicle moving on a long suspension bridge within multi-mode lock-in regions. *J. Wind Eng. Ind. Aerodyn.* **2023**, *234*, 105345. [CrossRef]
20. Liu, X.; Tan, J.; Long, S. Multi-axis fatigue load spectrum editing for automotive components using generalized S-transform. *Int. J. Fatigue* **2024**, *188*, 108503. [CrossRef]
21. Wu, T.; Qiu, W.; Yao, G.; Guo, Z. Vehicle ride comfort analysis on sea-crossing bridges under drift ice load. *Structures* **2023**, *47*, 846–861. [CrossRef]
22. *ISO2631-1:1997*; Mechanical Vibration and Shock—Evaluation of Human Exposure to Whole-Body Vibration—Part 1: General Requirements. International Organization for Standardization: Geneva, Switzerland, 1997.
23. *ISO2631-1:1985*; Evaluation of Human Exposure to Whole-Body Vibration—Part 1: General Requirements. International Organization for Standardization: Geneva, Switzerland, 1985.
24. He, H.; Sun, F.; Li, M. Current Status and Future Development of Integrated Transportation Technology in China. *Strateg. Study CAE* **2023**, *25*, 202–211. [CrossRef]
25. Ling, T.; Cao, R.; Deng, L.; He, W.; Wu, X.; Zhong, W. Dynamic impact of automated truck platooning on highway bridges. *Eng. Struct.* **2022**, *262*, 114326. [CrossRef]
26. Lai, Y.; Yan, F.; Yang, D. Key Design Technologies of Large-span Top-supported Hollow-web Beam-arch Composite Rigid Frame Bridges. *J. Highw. Transp. Res. Dev.* **2024**, *41*, 69–78. [CrossRef]
27. Yang, Y.; Wu, Y. A versatile element for analyzing vehicle-bridge interaction response. *Eng. Struct.* **2001**, *23*, 452–469. [CrossRef]
28. Michaltsos, G.T. Dynamic behaviour of a single-span beam subjected to loads moving with variable speeds. *J. Sound Vib.* **2002**, *258*, 359–372. [CrossRef]
29. Loprencipe, G.; Zoccali, P.; Cantisani, G. Effects of Vehicular Speed on the Assessment of Pavement Road Roughness. *Appl. Sci.* **2019**, *9*, 1783. [CrossRef]
30. Yan, L.; Hui, Q.; Min, L.; Qi, S.; Shen, X. Cable Breakage Effect and Safety Evaluation of Beam Arch Combination System Bridge. *Sci. Technol. Eng.* **2024**, *24*, 13960–13968. [CrossRef]
31. *JTG D60-2015*; General Code for Desigh of Highway Bridges and Culverts. China Communication Press: Beijing, China, 2004.
32. Wu, J.; Wang, Z.; Zhang, L.; Ding, X. Coordination Stability Control Strategy for Four-wheel-independent actuated Electric Vehicles. *J. Mech. Eng.* **2023**, *59*, 163–172. [CrossRef]
33. Guan, T.; Liu, D.; He, Y. Review on Development of Permanent Magnet In-Wheel Motors. *Trans. China Electrotech. Soc.* **2024**, *39*, 378–396. [CrossRef]
34. Li, J.; Gao, X.; Wang, P.; Zang, Z. Vibration Analysis of Electric Vehicle under the Action of Road and Switched Reluctance Motor. *J. Hunan Univ. (Nat. Sci.)* **2018**, *45*, 7–14. [CrossRef]
35. *ISO 8608:2016*; Mechanical Vibration—Road Surface Profiles—Reporting of Measured Data. International Organization for Standardization: Geneva, Switzerland, 2016.
36. Yang, Y.; Zhang, B.; Wang, T.; Xu, H.; Wu, Y. Two-axle test vehicle for bridges: Theory and applications. *Int. J. Mech. Sci.* **2019**, *152*, 51–62. [CrossRef]
37. Jiang, D.; Jiang, X.; Yi, J.; Lei, T. Dynamic Impact Effect of Separated Solid Plate Girder Bridge under Vehicle-Bridge Coupled Vibration. *J. Jilin Univ. (Eng. Technol. Ed.)* **2025**, 1–14. [CrossRef]